Catalysis Today 460 (2025) 115484

Contents lists available at ScienceDirect

Catalysis Today

journal homepage: www.elsevier.com/locate/cattod

Tuning the oxidative activity of copper-sites in Zr(IV)-C4 metal-organic frameworks

E. Vidal-Martin [a], M. Calles García [a], P.L. Arias [b], I. Oyarzabal [a,c], A. Rogalev [d], N.J. Yutronkie [d], I. Agirrezabal-Tellería [b], J. Sáiz [a], V. Petrenko [a,c], M. Gil-Calvo [b,*], R. Fernández De Luis [a,*]

[a] BCMaterials, BasqueCenter for Materials, Applications and Nanostructures, UPV/EHU Science Park, Leioa 48940, Spain
[b] Department of Chemical and EnvironmentalEngineering. School of Engineering, UPV/EHU, Bilbao, Spain
[c] IKERBASQUE, Basque Foundation for Science, Bilbao, Spain
[d] European Synchrotron Radiation Facility, Grenoble 38000, France

ARTICLE INFO

Keywords:
Halogen rich metal-organic frameworks
Copper
Coordination environment
Oxidative catalysis
Dopamine

ABSTRACT

Copper-based homogeneous catalysts have repeatedly demonstrated the critical importance of precisely controlling the coordination environment of active sites to fine-tune their activity, efficiency, or selectivity— a versatility that is still far from being achieved in traditional copper catalysts supported on zeolite or aluminosilicate. This is precisely where metal–organic frameworks (MOFs) can make a difference, offering structural and chemical versatility that enables precise control over their pore environments. In this research, we have employed three new halide rich zirconium microporous MOFs, to later on stabilize copper ions with bromide and thiol rich coordination environments. These copper-based catalysts have thoroughly evaluated over the dopamine oxidation via hydrogen peroxide activation. Following the elucidation of the copper site characteristics using a combination of EPR, UV-Vis, XPS, and XAS spectroscopic techniques, a clear correlation was established between these features and their ability to activate hydrogen peroxide and oxidise dopamine. This work highlights the significant catalytic advantage offered by copper active sites featuring bromide- and thiol-rich coordination environments within MOFs. This approach differs markedly from conventional strategies, which typically rely on nitrogen- or oxygen-based ligands to stabilise metal ions in these microporous materials

1. Introduction

Copper is one of the most versatile active centers in homogeneous catalysis and biocatalysis [1–3]. Although its functionality arises from several features, the versatility of its coordination sphere to adopt different conformations is one of its most important characteristics to modulate its catalytic activity [4,5]. In fact, the coordination environment of cooper sites is key not only to precisely tune its electronic structure, but also, to generate labile species that can easily leave and back the bonding sphere generating highly reactive positions [6,7]. In parallel, the same complexity also makes it challenging to modulate its coordination sphere in order to exert control over its redox and catalytic properties [8–10]. Metalloenzymes are an inspiring example of such control to stabilize metal-sites in specific spatial configurations [11–13]. Thus, an alteration of any of the amino acid residues that coordinate the metal placed into the heart of the metalloenzyme, affects drastically their function [11,14–16]. Inspired by nature, coordination chemists have achieved great success towards the development of chelating molecules able to stabilize copper ions with biomimetic-like coordination environments [17,18]. The chemistry of these chelating motifs has opened the room to extend the metal-coordination groups beyond the usual ones found in biocatalysts *(i.e. carboxyl, imidazole, thiol, amine…)*, endowing the copper ions with specific features and activity not found in nature [6,19]. In fact, the electronegativity of the binding groups forming part of the copper coordination environment is known to be one of the most important characteristics to modulate its electronic structure [15].

Despite the sophistication of copper sites found in homogeneous catalysis and biocatalysts, the stability of these complexes remains their Achilles heel with respect to their catalytic application and posterior recovery [20]. Successful heterogenization of copper sites in porous materials, such as zeolites and mesoporous silica, has enabled significant advances to mimic those found in copper metalloenzymes [21,22]. However, traditional inorganic porous materials offer limited

* Corresponding authors.
E-mail addresses: miryam.gil@ehu.eus (M. Gil-Calvo), fernandez@bcmaterials.net (R. Fernández De Luis).

https://doi.org/10.1016/j.cattod.2025.115484
Received 12 January 2025; Received in revised form 18 July 2025; Accepted 23 July 2025
Available online 29 July 2025

possibilities to fine-tune the coordination environment of copper ions, particularly when it comes to introducing diverse coordination groups beyond oxygen [23].

In this regard, the chemical diversity of a particular class of porous ordered materials called Metal-Organic Frameworks (MOFs) holds an enormous promise to stabilize copper sites with a fine control over their coordination environment [24]. MOFs are crystalline solids built from metal ions or clusters that are connected by organic linkers to form extended, ordered, and highly porous networks. Thanks to their (i) impressive and ordered porosity metrics and (ii) their versatility to be encoded with functionalities placed surgically at specific positions of their structures [25,26], The chemical encoding of amino acids or peptides in MOFs has opened the room to install copper ions exhibiting bioinspired coordination environments, and thus, specific catalytic functions [27−30]. [31]. Following a parallel approach, the decoration of the inorganic clusters of MOFs with single Cu-atom sites has enabled to drive CO_2 reduction reactions in complex gas and plasma media [32]. Nevertheless, most coordination groups used to stabilize copper ions in MOFs are based on highly electronegative atoms, such as oxygen (3.5) nitrogen (3.0) [18]. MOF catalysts featuring copper ions coordinated by intermediate to low electronegativity groups—such as bromine (2.8) or thiols (2.5)—remain scarce, despite well-established evidence that thiol coordination in copper-containing metalloproteins significantly modulate their catalytic activity in oxygen activation and electron transfer reactions involving the Cu(II)/Cu(I) redox couple [33,34].

In this research, we have employed bromosuccinic, dibromosuccinic, and dimercaptosuccinic C4-organic linkers to assemble three halogen- and chalcogen-rich Zr(IV)-based microporous MOFs (Scheme 1A) able to stabilize copper ions within a low electronegative coordination environment. Compared to MOF-801 – Zirconium fumarate [35,36] - or MIP-202 – zirconium aspartate [37] - reference materials, the dibromosuccinic and dimercapto-succinic C4-Zr-MOF variants synthesized in this study adopt a tetragonally compressed crystal structure, characterized by a narrow, -Br/-SH rich pore space, within which copper ions can be stabilized in a halogen/chalcogenide-rich coordination environment (Scheme 1B). In contrast, the cubic bromosuccinic-based MOF features a more open framework, similar to the one of MOF-801, less densely populated of bromine anions. Once the copper has been stabilized within their frameworks, it has been fully characterized by means of Infrared (IR), X-ray photoelectron (XPS), UV-Vis, electron

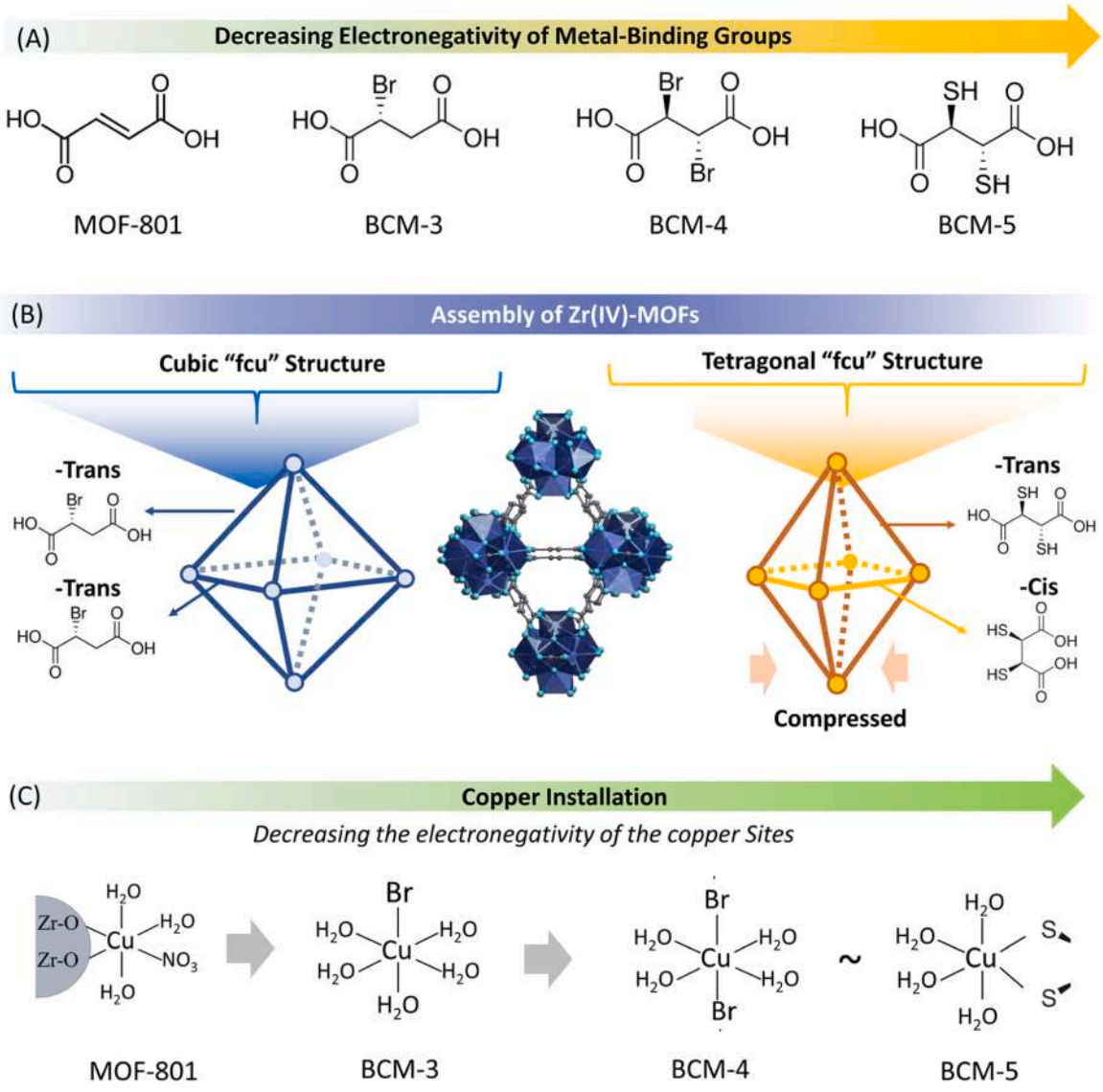

Scheme 1. A) Organic linkers employed to synthesize MOF-801, BCM-3, BCM-4 and BCM-5 Metal-Organic Frameworks materials. (B) Illustration of the structural differences observed for MOF-801 and BCM-3 cubic materials, and BCM-4 and BCM-5 tetragonal homologues. (C) Schematic representation of the possible coordination environments of copper ions incorporated into the various frameworks examined in this study.

paramagnetic (EPR) and X-ray absorption (XAS) spectroscopies in order to unravel their local structure (Scheme 1C).

Dopamine oxidation has been selected as a model reaction to investigate the impact of stabilizing copper ions in a -Br/-SH-rich environment and to assess how this influences the catalytic activity of our copper-based catalysts [38]. Dopamine oxidation is a redox-active process which is dependent on the pH or the presence of transition metal ions [39–42]. Overall, the reaction is highly relevant in neurochemistry – particularly in the context of oxidative stress and neurodegenerative diseases like Parkinson's – or as a chemical path to obtain multifunctional polydopamine coatings [43–47]. It is important to note that dopamine (DOP) can undergo auto-oxidation without the presence of any catalysts, in which the oxidative intermediate steps during the reaction are driven by reactive oxygen species, as superoxide anion (O_2^-), hydrogen peroxide (H_2O_2) or hydroxyl radicals (OH). The presence of Fenton-active metals in solution, such as copper and iron, adds further complexity to the DOP oxidation pathway [42]. In addition to their ability to directly coordinate dopamine via the catechol ring—thereby triggering electron transfer-driven oxidation—these metals can also activate oxygen and hydrogen peroxide. This leads to the generation of additional reactive oxygen species (ROS), which further accelerate dopamine transformation [48].

Thus, in this investigation, we employed the aforementioned chalcogenide/halogen-rich Metal-Organic Frameworks to stabilize copper ions within coordination environments partially composed of intermediate- to low-electronegativity donor atoms. Our objective was to assess how this deviation from conventional oxygen-based coordination spheres influences the oxidative behavior of the immobilized copper centers in the transformation of dopamine. Specifically, we focused on their activity during the initial oxidation step from DOP to dopamine-quinone (DQ), while also investigating their role in the broader transformation pathway—from DOP to 5,6-dihydroxyindole (DHI) and indole-5,6-quinone (IQ)—prior to the final polymerization into polydopamine.

2. Experimental

2.1. Reagents

All chemicals and solvents used were obtained commercially. Zirconium(IV) chloride (98 %, Glentham Life Sciences), bromosuccinic acid (96 %, ThermoScientific), 2,3-dibromosuccinic acid (98 %, ThermoFisher), (2R, 3S)-2,3-dimercaptosuccinic acid (95 %, Fluorochem), fumaric Acid (**99 %**, ThermoFisher), formic Acid (98 %, Labkem), copper(II) nitrate pentahydrate (99 %, Labkem), sodium hydroxide (97 %, Alfa Aesar) and methanol (99 %, Alfa Aesar), were used for the Zr-C4-MOFs synthesis. Dopamine (98 %, Sigma-Aldrich), 4-amineantipyrine (97 %, Alfa Aesar), H_2O_2 (30 % w/w in water, Sigma-Aldrich) and distilled water were employed for the wet oxidation catalysis assays. All the chemicals were used as provided.

2.2. Water based synthesis of Zr-C_4 metal-organic frameworks

Zr(IV)-fumarate/-bromosuccinate (c-fcu): The cubic variant of the Zr (IV) fumarate/-bromosuccinate (c-fcu) (hereafter denoted as BCM-3, BCM stands for Basque Center for Materials, Applications & Nanostructures) was synthesized by the hydrothermal reaction of $ZrCl_4$ and bromosuccinic acid. First, $ZrCl_4$ (1.71 g, 7.34 mmol) was dissolved in distilled water (15 mL). Then, separately, bromosuccinic acid (3.2614 g, 16.56 mmol) and formic acid (5 mL, 0.13 mmol) were dissolved in 26.7 mL of the same solvent. Afterwards, the $ZrCl_4$ solution was dropped slowly into the bromosuccinic and formic acids solution. The mixture was kept at

80 ºC for 24h in a screw-capped glass jar (100 mL). After the reactor was cooled down to room temperature, the sample was centrifuged (7830 rpm) and thoroughly washed two times with H_2O (30 mL) and subsequently two times with methanol (30 mL). Finally, BCM-3 was dried in an oven at 80 °C for approximately one day. It is important to note that 1H NMR data described in the following sections confirmed that the organic linker undergoes a partial debromination during the synthesis giving rise to the formation of a multivariate BCM-3 material with a 80 molar % of fumarate and a **20 %** of bromosuccinate organic linkers.

Zr(IV)- Dibromofumarate/bromofumarate/fumarate (t-fcu): The tetragonal variant of the multivariate Zr(IV)-bromofumarate/fumarate (hereafter denoted as BCM-4) was synthesized in the same conditions that BCM-3, but employing dibromosuccinic acid as the linker (4.5677 g, 16.56 mmol). Much like BCM-3, the organic linker undergoes a partial debromination process during the synthesis however, in this case it was much lower. The final materials show a multivariate mixture containing a 92.5 molar % of dibromosuccinate, a 2.75 % of bromofumarate and a 4.75 % of fumarate organic linkers. Like for BCM-3, ^{1}H NMR of the digested BCM-4 sample was employed to quantify the linkers.

Zr(IV)- Dimercaptosuccinate (t-fcu): The tetragonal variant of the Zr (IV)-dimercaptosuccinate compound (hereafter denoted as BCM-5) was obtained by a slightly modified synthesis path. Thus, first DMSA (0,6215 g, 3.41 mmol) was partially solubilized in 6.25 mL of a NaOH distilled water solution (0.137 g of NaOH, 3.43 mmol) at 80 ºC under vigorous stirring during 1 h. In a second step, $ZrCl_4$ (0.4275 g, 1.83 mmol) was dissolved in a formic acid (2 mL) solution in distilled water (6.25 mL). The $ZrCl_4$ solution was dropped slowly into the DMSA solution, and the mixture was heated at 100 ºC under reflux during 24 h. After the reaction was cooled down to room temperature, and a solid precipitate was isolated, washed, and activated as previously described above.

2.3. Copper integration and its stability assessment into the frameworks

Two parts of each activated material (100 mg/part) were immersed in a 50 mL Cu(II) aqueous solutions of 10 and 100 ppm concentrations respectively during 10 min. Copper(II) nitrate hydrate was employed as the copper source. Afterwards, the samples were recovered by centrifugation, washed with methanol, and dried at 50 ºC for one day. Here after, the samples after metalation will be referred as BCM-3@Cu10, BCM-3@Cu100, BCM-4@Cu10, BCM-4@Cu100, BCM-5@Cu10 and BCM-5@Cu100 referring to the concentration of the copper solution employed to functionalize the initial Z4-C4-MOF material. In order to unravel the copper stability in the frameworks under operation conditions, the metalated materials were immersed in hydrogen peroxide and hydrogen peroxide/dopamine solutions during one hour, and later recover, washed, dried, and characterized following the same protocols applied for the initial catalysts.

2.4. Characterization protocols

Most of the characterization protocols described in the following section were applied to the C4-MOF materials, before and after copper integration = , and after the catalysts were exposed to the reaction conditions employed for the dopamine oxidation reaction.

The X-ray diffraction (XRD) patterns were obtained using in a Panalytical X'pert Cu Kα diffractometer with 2θ range = 5–70 °, step size = 0.015 °, and exposure time = 10 s per step at room temperature. Panalytical X'pert is a polycrystalline sample diffractometer with θ–θ geometry, a programmable slit, and a secondary graphite monochromator adjusted to copper radiation and fast solid state PixCel detector adjusted to an 3.347° active length in 2θ (°). The equipment allows one to perform quality measurements for the subsequent data processing, at the level of full profile adjustments without/with a structural model.

Fourier transform infrared spectroscopy (FTIR) measurements were carried out using a Jasco FT/IR-6100 spectrometer in attenuated total reflectance mode (FTIR-ATR). The samples were measured in KBr

pellets. Each spectrum was recorded from 600 to 4000 cm^{-1} with a 1 cm^{-1} resolution. 64 scans were measured and averaged to obtain the final data.

In order to obtain the molar ratio of the organic building blocks of Zr-C4-MOFs, **proton nuclear magnetic resonance (^{1}H NMR)** analyses were performed in a Bruker AV500 equipped with a BBI probe and Z-axis gradients, operating at a frequency of 500 MHz for proton. For this purpose, 23 mg of the samples were digested overnight in a NaOH-deuterated water solution (1–0.7 mL) for BCM-3 and BCM-5. For BCM-4, 6 mg of sample were dissolved in a deuterated water solution with NaF (0.5–1 mL). Different procedures were chosen due to the stability of the ligands under the different conditions. The mixture was centrifugated at 7000 rpm, and the remnant solution recovered carefully with a syringe, preventing the uptake of the powdered material settled at the bottom of the centrifuge tube. First, the proton signals associated to the original ligands and of the dibrominated homologues after the synthesis were identified. Afterwards, the molar ratio between them, and the formic acid molecules was obtained for each material. All the process was performed with the aid of Mestre Nova software.

Thermogravimetric analyses (TGA) were performed to complement the ^{1}H NMR data. To this end, a Netzsch STA 449 F3 Jupiter thermobalance was employed in order to record the TGA/DSC simultaneous analyses between 25 and 700 °C, with a 5 °C min⁻1heating ramp, and under synthetic air atmosphere. Approximately 25 mg of each sample were employed for the analyses. Alumina crucibles were used as sample holders. As detailed in the results and discussion section, the combined analysis of the weight percentage associated to each degradation step of the Zr-C4-MOFs, together with the ligand molar ratios obtained from ^{1}H NMR, enabled proposing a chemical formula for each of the studies compounds before and after their metalation.

Carbon dioxide sorption isotherms were measured at 0 ºC with a High Pressure Quantachrome ISorb instrument. Approximately 150 mg of the samples were degassed at 120 °C in high vacuum for at least 12h prior to the measurement. The surface area values were obtained by the fittings of the adsorption data to a linearized result of the Brunauer–Emmett–Teller (BET) equation. **N_2-77K absorption isotherms** were acquired on a 3P Vapor-100C instrument. The samples were degassed in the same conditions reported for the CO_2 isotherms. A dose measuring mode was employed to acquire both the absorption and desorption branches of the isotherms.

The **UV-Vis spectra** of the metalated samples were measured using diffuse reflectance spectroscopy (DRS). The measurements were carried out using an ultraviolet, visible, and near-infrared V-770 Jasco spectrophotometer, equipped with a 150 mm diameter integrating sphere coated with Spectralon, with wavelength range of 200–1400 nm and spectral resolution of 1 nm. To remove the background and noise, a Spectralon reference was used to measure the **100 %** reflectance and internal attenuators to determine zero reflectance.

All **X-ray Photoelectron Spectroscopy** (XPS) spectra were acquired using a monochromatic X-ray source producing Al Kα radiation ($h\nu$ = 1486.6 eV) and were recorded using a SPECS PHOIBOS 150 analyzer. The take-off angle of the photoelectrons was 90° with respect to the specimen. The energy resolution was 0.6 eV. Individual high-resolution spectra were acquired at 40 eV. Binding energies were calibrated against the silver Ag 3d3/2 binding energy.

Electron Paramagnetic spectroscopy (EPR) spectra were recorded at room temperature using a Bruker ELEXSYS 500 spectrometer (X and Q bands). The spectrometer was equipped with a superhigh-Q resonator ER-4123-SHQ and the samples were placed in quartz tubes. All samples contained similar amounts of material and were packed equally in order to establish a qualitative comparison. The magnetic field was calibrated by an NMR probe and the frequency inside the cavity (~9.395 GHz) was determined with an integrated MW-frequency.

X-ray Absorption Spectroscopy (XAS) measurements were performed at the ID12 beamline of the European Synchrotron Radiation Facility (ESRF). X-ray Absorption Near Structure (XANES) spectra were collected at the Cu K-edge on pressed powder samples of BCM3 and BCM4 using total florescence yield detection mode. The energy of the X-ray beam was tuned using the second harmonic of a HELIOS type undulator (HU-52) and Si⟨111⟩ double crystal monochromator.

2.5. Catalytic Wet Peroxide Oxidation of Dopamine (CWPO)

The catalytic activity of BCM-3@Cu was optimized and measured via a chromogenic reaction of the substrate with 4-aminoantypirine (4-AP). Later, these optimized conditions were employed to test BCM-4@Cu and BCM-5@Cu catalysts. To this end, the effect of the catalyst dosage, the hydrogen peroxide addition, and the ionic strength of the media were studied. In a typical reaction, 100 μL of a dopamine (DOP) aqueous solution (1mg·mL^{-1}), 400 μL of 4-AP aqueous solution (1 mg·mL^{-1}) and 100 μL of the catalyst dispersion in water (1 mg·mL^{-1}). As a last step, 20 μL of H_2O_2 were added to initiate the oxidation. The volume of the reaction was completed with distilled water until a total of 1 mL. The time dependence of the absorbance of the solution was measured by UV-Vis at 510 nm. Each of the reactions where fitted to a first order kinetic model to obtain the k-rate of the substrate oxidation. Once the reaction conditions that induce an intermediate conversion of the substrate for the above described conditions were established, the influence of DOP concentration on the reaction kinetics was then studied. To this end, a series of 100 μL aqueous solutions of DOP ranging from concentrations of 0.1–2 mg·mL^{-1} were added to reaction media. The quantities of the rest of the materials/reagents were maintained the same. For these reactions, the K_M and V_{max} kinetic parameters were obtained with the Michaelis-Menten fitting described by the Eq. (1):

$$V_0 = V_{\max}\frac{[S]}{K_M + [S]} \quad (1)$$

where V_0 is the apparent initial catalytic rate, KM is the apparent Michaelis-Menten constant, V_{max} is the maximum apparent initial reaction rate and [S] is the substrate concentration. In addition, we employed the methods reported by J. Wang et. al. [Ref 82] The crystallographic densities of the BCM materials were taken as the nanozyme density to calculate the mass of a single nanozyme particle, as well as the nanozyme concentration *[E]* (mM). For all the reactions, the activity was normalized to the copper content of the catalysts in order to determine the turn over frequency (TOF) of the reactions. This approach allows comparing rigorously the activity of the copper sites for each of the studied catalysts.

It is important to note that measuring the UV-Vis abs. at 510 nm arising from the complex formed between the oxidation product of the substrates and the 4-AP does not enable quantifying the reaction product. Thus, a protocol for the semiquantitative estimation of the product concentration has been developed. First, we have assumed that a highly concentrated copper nitrate solution (100 mg·L^{-1}) employed as a homogeneous catalyst would induce almost complete dopamine conversion. Hence, the CWPO was performed by increasing progressively the concentration of DOP and obtaining a linear tendency that correlates the absorbance as a function of DOP concentration recorded at 510 nm. The absorbance values obtained when employing a 100 mg·L^{-1} copper solution as homogeneous catalyst exceed by far the ones obtained when employing MOFs as heterogeneous catalysts. This finding points towards a high conversion degree of the substrates when employing −100 ppm of Copper nitrate homogeneous catalyst. When fitting the data, a relatively good correlation is obtained. Still, significant background absorbance arising from the secondary oxidation of 4-aminoantipyrine is obtained in the calibration curve (Figure S5). That is, the absorbance value at 510 nm obtained for a reaction without substrate but with 4-AP (i.e. 0.186) is similar to the one read for DOP. In any case, this background signal is far lower than the signal that is obtained during the DOP oxidation, so we have opted to overlook it during the calculation of the product concentration. All in all, the fittings obtained from the Abs. vs. substrate concentration curves give semiquantitative estimations of the

conversion, but they are still more accurate than comparing the performance of the catalyst on the basis of absorbance values.

The full oxidation of dopamine was followed by liquid chromatography. To this end, 4-AP and NaCl were removed from the reaction media. In a standard reaction setup, 2.5 L of a

1 mg·mL^{-1} dispersion of the catalysts, 5 mL of a 1 mg·mL^{-1} dopamine solution and 750 μL of H_2O_2 were added to the reactor under continuous stirring conditions. The chromatographic analyses of the dopamine and of its degradation products were performed using an Agilent Infinity 1260 chromatographic system, equipped with a Diode Array Detector (DAD) set to monitor at a wavelength of 280 nm for dopamine. The system was equipped with an InfinityLab Poroshell 120 EC-C18 column (3.0 × 100 mm, 2.7 μm particle size) coupled with a guard column of the same material. Mobile phase A was 0.1 % (v/v) formic acid in water and mobile phase B was acetonitrile containing 0.1 % (v/v) formic acid. The chromatographic gradient began with 0 % of mobile phase B at 0.00 min. From 0.00–7.00 min, the percentage of mobile phase B increased linearly to 60 %. At 7.01 min, a rapid step increase brought mobile phase B to 100 %, which was maintained isocratically from 7.01 to 8.00 min. Finally, the gradient returned to 0 % mobile phase B at 8.00 min and was held at this composition until 15.00 min to re-equilibrate the column. The mobile phase flow rate was maintained at 0.5 mL/min, and the column temperature was set to 40 °C to ensure consistent retention times and peak resolution. Sample injection volumes were 5 μL.

3. Results and discussion

3.1. Characterization of C4-MOF materials

As detailed in the experimental section, the BCM-3, BCM-4 and BCM-5 materials were obtained after the hydrothermal reaction of the organic linkers and zirconium chloride in water, and subsequently analyzed by powder X-ray diffraction, as illustrated in the Fig. 1a. The first visual inspection of the PXRD data reveals that the Zr-C4-MOFs assembled from bromosuccinic (BCM-3), versus the ones crystallized from dibromosuccinic (BCM-4) and dimercaptosussinic (BCM-5) acids, exhibit two different diffraction patterns (Fig. 1a). The XRD-pattern of BCM-3 is similar to the one reported for MOF-801 [35], MIP-202 [37] or

MIP-205 [49] materials, exhibiting the two most intense diffraction maxima located at low *2θ(°)* values (i.e. 8.65 and 9.95 °). In contrast, BCM-4 and BCM-5 exhibit a PXRD signature characterized by a single intense maximum (i.e. 8.5°), followed by a second signal of much lower intensity located at 9.2° approximately. Given that any change on the position and intensity of the diffraction maxima is intrinsically linked to the structure of the C4-MOF, we came back to bibliography to double-check the structural models reported for zirconium MOFs constructed from C4-linkers.

As already mentioned, until recently, the crystal structures of zirconium MOFs assembled from C4-dicarboxylate linkers had adopted the archetypal cubic symmetry (S.G. = *Pn*-3), as to those seen in MOF-801 [35,36], MIP-202 and MIP-205 [50] family. The crystal structure of these materials is assembled from the connection of $Zr_6(\mu_3\text{-}O)_4(\mu_3\text{-}OH)_4$ hexameric oxo-clusters through twelve organic linkers. Later, the structural dynamics of Zr-MOF assembled from malic, succinic and fumaric linkers were reported by S. Wang et al [50]. were the connectivity of the $Zr_6(\mu_3\text{-}O)_4(\mu_3\text{-}OH)_4$ unit was reduced from twelve to eight, giving rise to a loss on the symmetry of the framework to the orthorhombic *Immm* space group. Orthorhombic variants of C4- MOFs share both C4-linkers and formate anions as the bridging units to connect the zirconium clusters into a three-dimensional flexible framework that is adapted to the adsorption/desorption of different solvents. Recently, the cubic (S.G. = *F*23) and the hexagonal (S.G. = *P*63/*mmc* – *hcp topology*) variants of Zr-C4-MOFs were reported when thiomalic acid is employed

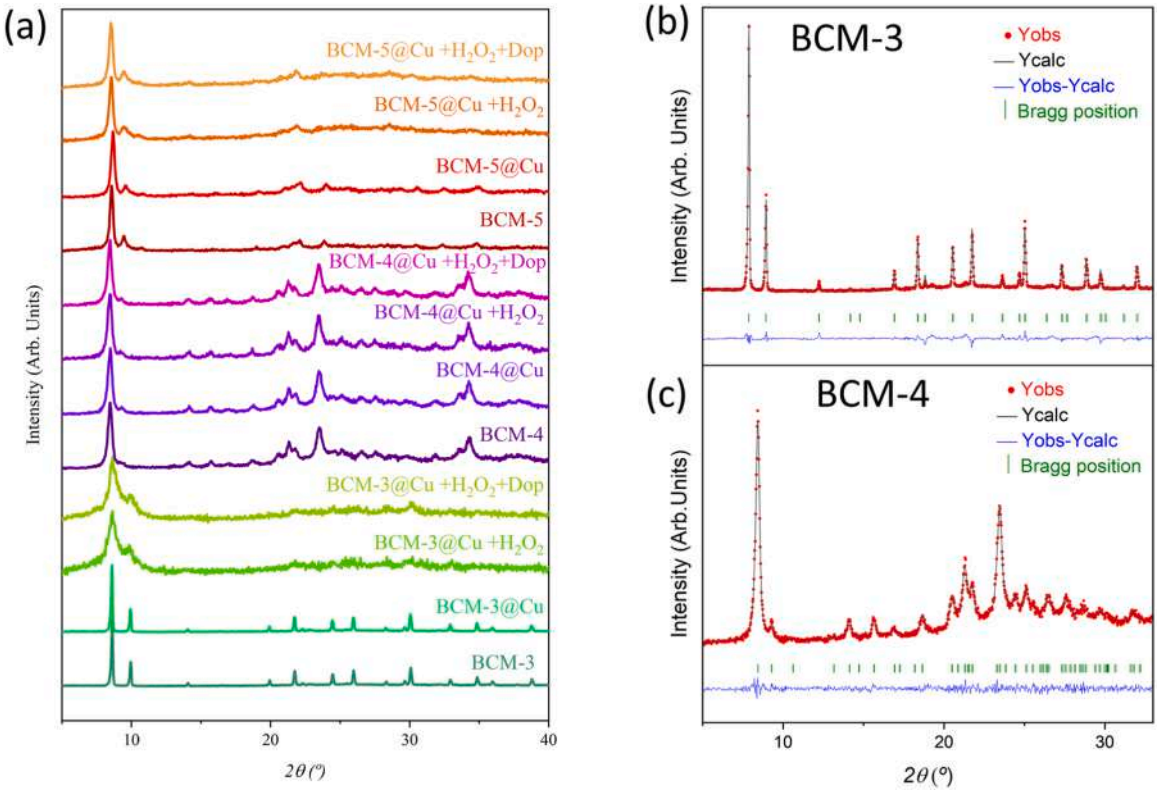

Fig. 1. (a) XRD-patterns of BCM-3, BCM-4 and BCM-5 before and after copper metalation, and after exposing the catalysts to H_2O_2 and Dopamine solutions employed for catalytic reactions. For sake of simplicity, only the XRD-data for the samples doped with a 100-ppm copper solution are shown. (b-c) Full profile fitting of the XRD-data for (b) BCM-3 and (c) BCM-4. Data for BCM-5 is shown in supplementary information file.

to assemble the corresponding three-dimensional porous networks [51]. The structure of the cubic phase with a *F*23 symmetry is very similar to the one reported for

MOF-801, but exhibit a positional disorder on the organic linkers imposed by symmetry. The formation of the hexagonal variant was highly dependent on the addiction of formic acid as modulator in the synthesis media, which induces the collapse of two Zr_6 units linked via μ_2-OH groups into double Zr_{12} units. These SBUs are connected giving rise to hexagonal metal-organic layers with an "hxl" topology. Those are further connected via the thiomalate linkers in the "c" crystallographic direction to generate a three-dimensional structure with an "hcp" topology homologue to the one already reported for UiO-67 or UiO-66 materials [52,53].

As a first step in the analysis, we compared the experimental data of the BCM-3 to BCM-5 compounds studied in this work with the patterns simulated from the cubic, hexagonal and orthorombic crystal structures of Zr-C4-MOFs (Figure S1). From the initial visual inspection of the data, we found clear similarities between the pattern for BCM-3 and the ones already reported for BCM-1 (*F*23) or MOF-801 cubic materials. The profile matching analysis for

BCM-3 indicates that the XRD data fits with both cubic models, giving rise to a cell parameter (a = 17.850(1) Å) very close to the one reported for MOF-801 or BCM-1 (Fig. 1b). Thus, the crystal structure of BCM-3 is likely to be build up from $Zr_6(\mu_3\text{-}O)_4(\mu_3\text{-}OH)_4$ connected through twelve organic linkers (Scheme 1b).

In comparison to BCM-3, the XRD data of BCM-4 and BCM-5 slightly deviate from the cubic symmetry. A similar mismatch is shown from the comparison with the simulated patterns of the orthorhombic and the hexagonal variants. The full profile matching starting from the cell parameters and the space group symmetry of orthorhombic and hexagonal variants further confirms this mismatch. In line with these findings, BCM-4 and BCM-5 do not show structural flexibility upon thermal treatment or solvent exchange like that exhibited in orthorhombic MIP-203. A symmetry reduction from the cubic *F*23 to a tetragonal crystallographic cell with a slightly compressed "c" parameter is needed to fit the experimental data (a = b = 13.459(3) Å and c = 16.685(4) Å; Scheme 1b).

Further, the analysis of the crystallographic systematic absences suggests *P*4*nc* as a possible space group for BCM-4 and BCM-5 materials. When correlating the crystallographic cells of the cubic *F*23 or *Pn*3 variants with the one of the tetragonal phases, it is clear that the later structure is compressed along the c crystallographic axis, while the a and b parameters are expanded in comparison to the parent cubic material. This compression gives rise to a reduction of the pore window and volume of the structure. A preliminary analysis of the synchrotron radiation-based single-crystal X-ray diffraction data indicates that the dibromosuccinic linkers adopt both *trans* and *cis* conformations within the structure. The *cis* configuration leads to a reduced cluster-to-cluster distance along one of the crystallographic planes, resulting in a symmetry reduction and an overall compression of the framework, as illustrated in Scheme 1b. Notably, full-profile fitting of the XRD data using a unit cell with parameters $a = b = 13.459(3)$ Å, $c = 16.685(4)$ Å, and a *Pn*4*c* space group yields an accurate match with the experimental diffraction pattern (Fig. 1c).

It is important to note that the copper metalation of the materials does not affect the XRD fingerprint of the materials, and thus, the patterns do not show displacement of the diffraction maxima, neither significant variations on their relative intensities. While exposure to H_2O_2 and dopamine solutions does not affect the XRD signal of BCM-4 and BCM-5, it causes a significant reduction in the crystallinity of BCM-3. Even though, the most intense diffraction maxima remain at their original positions suggetsing that the long-range structural order of BCM-3 is still preserved under catalytic conditions.

^{1}H NMR analyses further help to understand the composition of the Zr-C4-MOFs by quantifying the proton signal of the organic linkers after the MOF-digestion in basic conditions. The spectra of the deuterated solution obtained from the digested BCM-3 and BCM-4 mismatch the ones of the organic linkers employed for their synthesis (Fig. 2a and Table 1). The digestion conditions of the MOFs were varied to confirm that debromination occurs during MOF synthesis rather than as a result of the digestion process itself. Since bromide is an easy leaving group, fumaric acid was initially identified as the major organic component (i.e. **80 %**) of BCM-3 after the debromination of the initial linker during the synthesis. As secondary linker, minor molar percentages of the initial bromosuccinate linker (i.e. **20 %**), was also identified. In addition, the ^{1}H NMR spectrum of bromosuccinate shows signal splitting, attributed to slight chiral behavior arising from the presence of an asymmetric carbon in its structure. As a result, the accuracy of the molar quantification of the different linkers in BCM-3 is partially limited. Currently, we are softening the synthesis conditions of BCM-3 to corroborate if the debromination degree can be modulated, and in turn, the crystallization of the final framework affected. A similar partial debromination of the linker is found for BCM-4, where the ^{1}H NMR spectra indicate that dibromosuccinic acid has been partially transformed to bromofumarate (**2.75 %**) and fumarate (**4.75 %**) linkers. Here the debromination is significantly lower than for bromosuccinic acid, and dibromosuccinate

(**92.5 %**) is the major component of BCM-4. For BCM-5, assembled from dimercaptosuccinate, ^{1}H NMR spectra are in an agreement to what would be expected for this molecule. Assuming that the formic acid content is negligible, the molar ratios of the organic linkers obtained from ^{1}H NMR (Fig. 2a) were employed to suggest the average formula of Zr-C4-MOFs, assuming that the tetragonally distorted compounds maintain the same connectivity than the archetypal "fcu" cubic framework, as suggested by the TGA analyses (Table 1).

X-ray fluorescence (XRF) was employed to offer insights into composition of the Zr-C4-MOFs (Fig. 2 and Table 1). First, XRF data suggests that the content of Br of BCM-3 and BCM-4 exceeds the one expected if the linkers detected by ^{1}H NMR are solely employed to propose a chemical formula. Thus, given the acidic synthesis conditions, bromine could be stabilized as bromidic acid in the pores of BCM-3 and BCM-4. For BCM-5, the Sulphur content determined by elemental analysis is in close to the calculated one from its average formula (Table 1). XRF analysis confirms that the oxidative conditions employed during catalysis induce a significant release of copper ions from the framework (Fig. 2c). A smaller, but still noticeable, copper loss occurs when the catalysts are exposed to dopamine. Further exposure of the materials to hydrogen peroxide and/or dopamine does not cause additional copper leaching. Therefore, it can be concluded that the remaining copper ions after catalyst exposure to reaction conditions are strongly bound to the framework.

Thermogravimetric analyses were employed to evaluate the degree of linker defects of the materials, and in parallel, to estimate their thermal stability (Fig. 2d, Figure S2a and Figure S2b). All the studied materials show a similar three-step thermal decomposition profile accounting for their dehydration (20–150 °C), and a two-step organic linkers calcination process (150–250 °C and 250–600 °C) [54–57]. Indeed, for BCM-5, the experimental weight loss fits quite well if an ideal non-defective $Zr_6O_4(OH)_4(L4)_6$ formula is proposed assuming the full calcination of the organic components gives rise to the crystallization of ZrO_2 (Figure S2b). The same assumption for BCM-3 and BCM-4 is not fully true, since the experimental value surpass significantly the calculated one. The matching between the experimental and calculated data needs for the assumption of HBr molecules arising from the debromination of the linkers trapped within their pore space.

Revisiting the thermogravimetric profile, the three decomposition steps now can be clearly assigned to the dehydration of the samples, the release of the HBr molecules, and last, the calcination of the organic linkers. Of note is the fact that combining the information arising from ^{1}H NMR, XRF and TGA, it can be concluded that not all the bromine ions released from the organic linkers are trapped in the pore space of BCM-3. This is true for BCM-4, where the HBr molecules coming from the partial debromination of the dibromosuccinate linkers are found in the

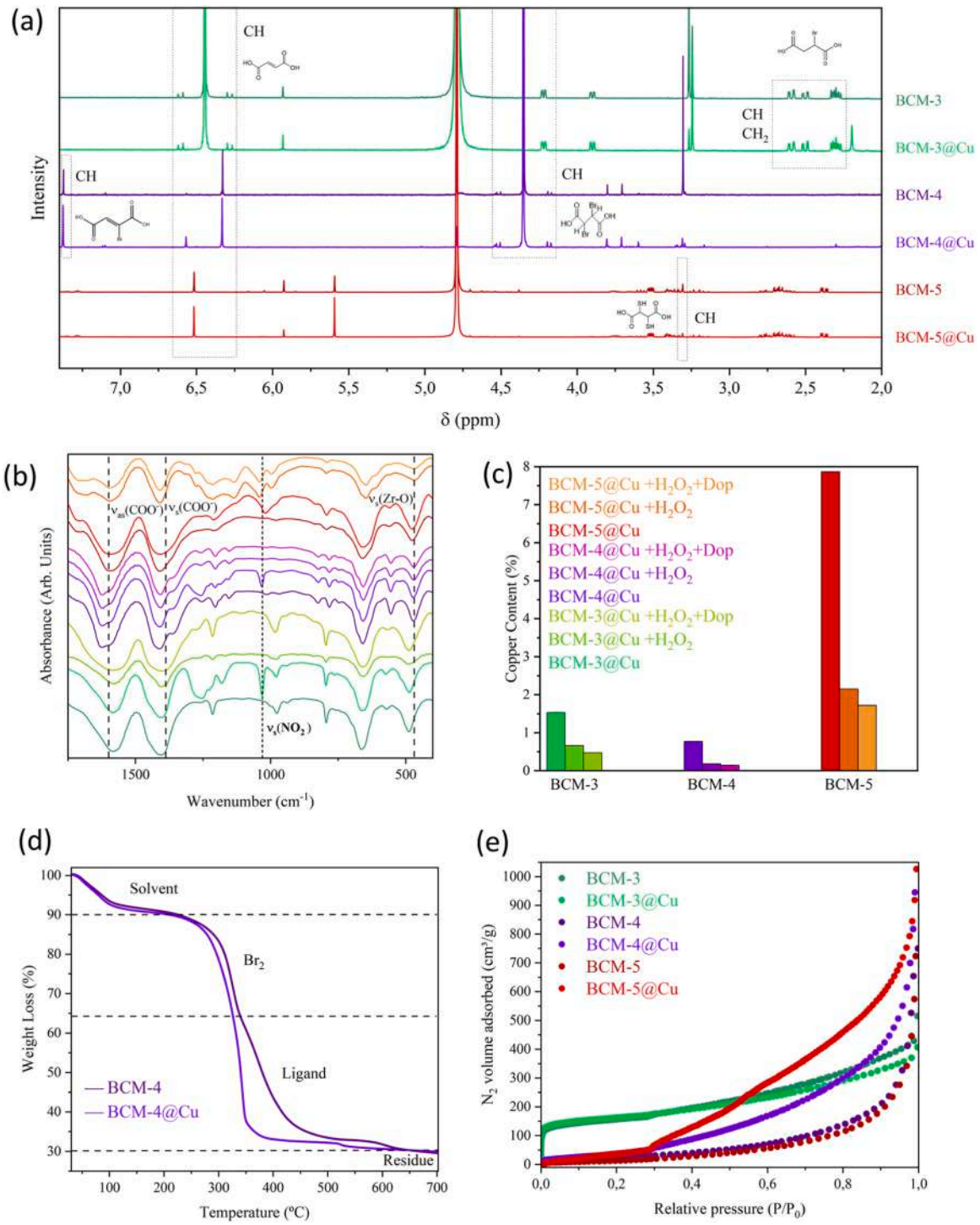

Fig. 2. (a) ^{1}H NMR and (b) IR spectra of BCM-3, BCM-4, and BCM-5 before and after copper metalation; IR also includes spectra after exposure to H_2O_2 and H_2O_2/dopamine. (c) Copper content before and after reaction conditions. (d) TGA curves of BCM-4 pre- and post-metalation. (e) N_2 adsorption isotherms at 77 K for all materials before and after metalation. The figure shows only the data for the samples metallated under 100 ppm copper solution.

material. The overall tendencies observed in the chemical formula of the compounds agrees with the structural information, since the compressed structure of BCM-4 would trap more effectively the HBr during the organic linkers debromination more effectively than the open cubic structure of BCM-3. In line with the previous results for XRF data, the copper metalation of BCM-3 further reduces its Br content, whilst the one of BCM-4 remains approximately stable. In comparison, BCM-5 exhibits a quite stable composition without Sulphur loss during the synthesis or metalation stages (Table 1). The thermogravimetric profile is slightly affected after the copper metalation, but still maintain approximately the same overall weight lost compared to the as-synthesized materials. In particular, the three mass losses are clearly distinguishable in the undoped materials, whereas only two are evident in the doped counterparts. The unobserved mass loss corresponds to the HBr molecules retained in the pores, since they are eliminated from the structure during doping.

The porosity of BCM-3, BCM-4 and BCM-5 was studied by means of CO_2-273K and N_2-77K isotherms (Figure S3). The profile of the

Table 1
- Chemical formula obtained from XRF, ^{1}H NMR and TGA analyses.

		Calculated (%)			Experimental (%)		
Code	Formula	Zr	Br	Cu	Zr	Br	Cu
BCM3	$Zr_6O_4(OH)_4(L1)_{4.64}(L2)_{1.17}(AF_2)_{0.093}(HBr)_{0.04}$	85.0	15.0	-	84.9	15.1	-
BCM3@Cu100	$Zr_6O_4(OH)_4(L1)_{4.64}(L2)_{0.37}Cu_{0.39}$	91.0	4.9	4.1	91.0	5.0	4.1
BCM4	$Zr_6O_4(OH)_4(L4)_{5.45}(L3)_{0.16}(L1)_{0.28}(HCOO)_{0.11}(HBr)_{0.77}$	36.7	63.3	-	36.7	63.3	-
BCM4@Cu100	$Zr_6O_4(OH)_4(L4)_{5.45}(L3)_{0.22}(L1)_{0.27}(AF_2)_{0.05}Cu_{0.39}$	37.5	60.8	1.7	42.6	55.6	1.7
BCM5	$Zr_6O_4(OH)_4(L5)_6$	-	-	-	-	-	-
BCM5@Cu100	$Zr_6O_4(OH)_4(L5)_6Cu_{0.25}$	97.2	-	2.8	97.2	-	2.8

L1- Fumarate, L2 – Bromosuccinate, L3 = Bromofumarate, L4 = Dibromosuccinate, L5 = Dimercaptosuccinate

isotherms confirms the microporous nature of the materials, but with significant differences on their surface area. In fact, BCM-3, which exhibit an "open" cubic crystal structure, shows a surface area slightly below the one reported in previous studies for MOF-801. This is understandable, since BCM-3 has a 20 % of molar content of bromosuccinate linkers in its structure, in addition to the hydro bromidic acid molecules trapped within its pore space. BCM-4 and BCM-5 exhibit a surface area value three-fold lower than BCM-3 due to the compression of their structure along the "c" axis together with the presence of bromide and thiol groups decorating their organic linkers. N_2 adsorption isotherms at 77 K were recorded for both non-metallated and copper-metallated materials to assess whether copper incorporation affects porosity (Fig. 2e). The similarity if the isotherms for BCM-3 and BCM-3@Cu indicate that the microporosity of the material is retained after the copper installation, with a pore size distribution centered around 6 Å and surface areas close to 500 m^2/g for both samples. However, for BCM-4 and BCM-5, the narrow pore sizes make N_2 an unsuitable probe molecule to accurately study their microporous structure, as confirmed by CO_2 adsorption isotherms. Although a slight increase in N_2 adsorption at low partial pressures was observed—resulting in surface areas of approximately 90 m^2/g for BCM-4 and 210 m^2/g for BCM-5—the low-pressure data are not reliable enough to accurately determine pore sizes $\leq$ 4 Å. It is interesting to note that N_2 adsorption at high partial pressures is significantly affected when the materials are doped with copper, likely due to stronger adsorbate–adsorbent interactions established on the MOF particle surfaces under these conditions.

Infrared spectroscopy allows us to shed more light on the nature of our materials, and in addition, on their copper adsorption mechanism (Fig. 2e). Our C4-MOFs share many IR absorption bands related with the vibrational modes common of their organic linkers. Just to mention some of them, the absorption bands associated to the asymmetric and symmetric stretching vibrational modes of COO^- groups are found between 1650 and 1350 cm^{-1}. At higher wavenumber values (~1700 – 1710 cm^{-1}), a weak band ascribed to the υ(C═O) vibrational mode is found. This signature confirms the presence of uncoordinated carboxyl groups, and hence, some defectivity within the network of the studied materials. Other signals, as the symmetric (i.e. 1050–1020 cm^{-1}) and asymmetric (i.e. 970–950 cm^{-1}) δ vibration of C-H bonds are also observed [58]. In addition to these common vibrational modes, each material shows some characteristic IR-fingerprints arising from the brominated and thiol-based organic linkers. Still, the variations observed before and after copper installation are limited to the attenuation of the weak absorption band located at 2000 cm^{-1} that is linked to the stretching vibrational mode of thiol groups for BCM-5, and the appearance of a new sharp and intense signal close to 1020 cm^{-1}. After a careful analysis, the IR-band was associated to the nitrate anions coming from the copper nitrate salt employed to metallate the materials. The position of the signal suggests a monodentate binding mode of the nitrate anions, likely bonded to the copper ions stabilized in the framework (Fig. 2b). It is interesting to note that the IR-extra signals arising from the copper metalation, specially these associated to nitrate groups, disappear after the materials are exposed to hydrogen peroxide, and hydrogen peroxide/dopamine solutions. This fact is likely to be correlated with the loss of these copper species weakly bonded to the structure of BCM compounds. In addition, the appearance of new IR-signals close to 1200 and 1000 cm^{-1} for BCM-5 samples after their exposure to H_2O_2, can be attributed to symmetric and asymmetric stretching vibrations of S-O bonds, which indirectly suggest a partial oxidation of thiol to sulfonic groups in the structure [51]. Once the structural and chemical stability of our microporous Zr-C4-MOFs had been confirmed after the copper installation, we moved to test the oxidative catalytic activity of each of the studied materials.

3.2. Catalytic Wet Peroxide Oxidation (CWPO) of dopamine

This section evaluates the performance of our copper catalysts, with its findings serving as a foundation for the next section. There, we explore how the ability to activate H_2O_2—and consequently drive the Catalytic Wet Peroxide Oxidation (CWPO) of dopamine (DOP)—is connected to the characteristics of the copper ions embedded within Zr-C4-MOFs. The reaction has been studied from two perspectives, the first, employing a colorimetric protocol that enables following only the first oxidation step of DOP substrate, and the second, where the complete reaction has been followed by liquid chromatography. All the catalysts studied in this section are the ones doped with a 100-ppm copper solution.

3.2.1. Studying the first oxidation step of CWPO of DOP

As illustrated in the Fig. 3a, if the copper sites are able to activate H_2O_2 and oxidize DOP, they will generate a reactive quinone intermediate that will bind 4-aminoantipyrine (4-AP) to generate a colored product. This can be easily follow up by liquid UV-Vis spectroscopy. (Fig. 3a) [59,60].

BCM-3@Cu catalyst has been selected to optimize the reaction conditions by means of varying the dosage of the catalyst, the ionic strength of the media, and the addition of 4-AP. The absorbance of the solution at 540 nm -the maximum-absorbance of the complex formed by the DOP and 4-AP during oxidation- of the after 5 min was recorded as a reference. At this time of reaction, the maximum of absorbance has been reached for most of the experimental conditions. As shown in the Fig. 3b, increasing the catalyst́s dosage has a slight detrimental effect on the efficiency of the reaction, which can be attributed to the overoxidation of the primary products and the reduction of the overall absorbance of the solution. As reported in previous studies, increasing the ionic strength of the media improved the conversion efficiency of the CWPO (Fig. 3b). Last but not least, increasing the addition of 4-AP improves as well the final absorbance value, since it is likely to promote the formation of the colored complex at the fixed time of the reaction where the absorbance has been recorded (Fig. 3b).

Once optimized the conditions for CWPO, in the following reactions the addition of the catalysts (50 μL), NaCl (300 μL) and 4-AP (300 μL) have been fixed, whilst the concentration of the DOP substrate has been systematically increased. It is worth noting that the absorbance values have been qualitatively converted into DOP concentration (see supplementary material for a detailed information). In addition, the conversion obtained for each of the catalysts has been normalized to their copper content in order to obtain the turn over frequency (TOF) values that enables a reliable comparison of the activity of each copped site installed

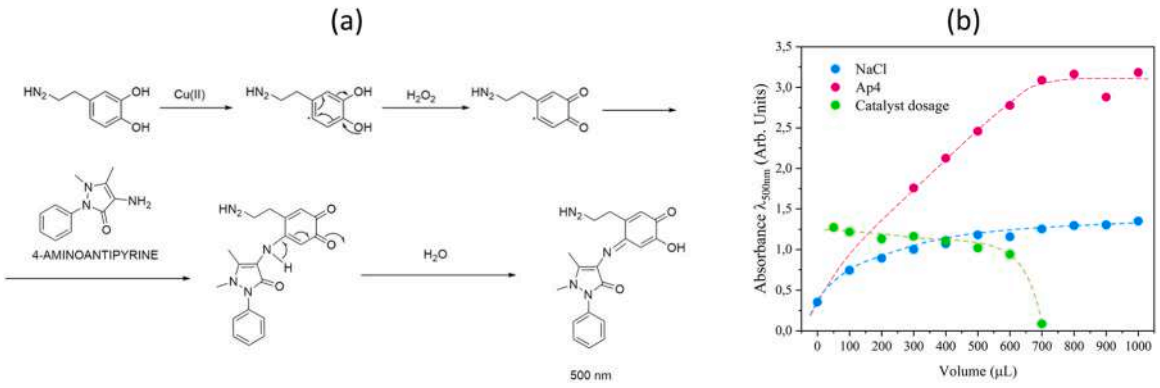

Fig. 3. a) Chromogenic reaction for the study of the first step pf the CWPO of dopamine. b) Absorbance dependence of the reaction conditions (i.e. catalyst, NaCl and 4AP dosages).

into the

Zr-C4-MOFs. We have assumed that the copper content is the one that have been determined after the exposition of the initial metallated catalysts to hydrogen peroxide and DOP, as illustrated in the Fig. 1c.

First, it is important to mention that the oxidation reaction of DOP is quite fast, and most of the conversion is achieved before the first five minutes of the reaction. At a first sight, the results obtained from the different reactions performed with increasing DOP concentrations does not show a clear link between the copper content of the catalysts and the final conversion (Figure S4). In turn, the opposite trend is observed when the efficiency is compared in terms of the activity per metal site (i.e. TOF) (Fig. 4a-c). For instance, BCM-5@Cu, which shows the highest copper content of the three catalysts, exhibits the lowest activity within the first five minutes of reaction monitored in this experiment. A slight increase on the conversion when the DOP concentration is increased is detected for BCM-5@Cu, but still far from the conversion rates of the BCM-3 and BCM-4 brominated variants. A very low activity for this first oxidation step of DOP was observed for copper doped MOF-801, that was taken as a reference catalyst that stabilize copper ions with a coordination sphere fully composed of oxygen atoms. In comparison, the and kinetics for the overall conversion and the TOF per metal site of BCM-4 for this first step of DOP oxidation are better that the ones of BCM-3. Similar conclusions are drawn when the data was fitted to Michaelis-Menten model (Fig. 4d).

As shown in the Fig. 4d, the profile of the Michaelis-Menten curves are similar for BCM-3 and BCM-4, which show a fast increase of the kinetics at low DOP concentration. The V_{max} and K_M values extracted from the fittings are detailed in the Table 2. From these data, it can be concluded that for the above-mentioned catalysts, the higher the V_{max}, the higher the [DOP] saturation of the active sites. The $K_{Mi>}$ and V_{max} values confirm that the copper sites in BCM-4 are the most effective at activating H_2O_2 and initiating the first step of DOP oxidation, followed by BCM-3 (Table 2). In contrast, BCM-5 shows very limited reactivity during the early stages. However, a continuous increase in color intensity is observed, eventually stabilizing at absorbance values similar to those of BCM-3 and BCM-4 when the reaction is extended to

24h [31]. The comparison between K_M and V_{max} indicates that BCM-4@Cu catalyst breaks the general tendency observed for the other materials studied in this work. That is, BCM-4@Cu exhibits a higher saturation value of its active sites.

To gain further insight into the reaction mechanisms of our catalysts, dimethyl sulfoxide and hexavalent chromium were used as scavengers for hydroxyl radicals and electrons, respectively. The activity of BCM-3 and BCM-5 remained largely unaffected by the presence of these scavengers. However, a slight increase in activity was observed for BCM-5 in the presence of hexavalent chromium. In contrast, the scavenging of hydroxyl radicals showed no appreciable impact. This suggests that reactive oxygen species (ROS) other than hydroxyl radicals may be involved in the catalytic process, and that electron trapping could help extend their lifetime and enhance catalytic efficiency [55].

By contrast, the addition of scavengers to the reaction medium of BCM-4 clearly affected its performance. The presence of electron scavengers significantly attenuated the activity, indicating that a Cu(II)/Cu(I) redox cycle plays a central role in the oxidation of DOP. Interestingly, an increase in activity was observed upon hydroxyl radical scavenging. Although counterintuitive, this effect could be attributed to a shift in the H_2O_2 activation pathway that favours the formation of more controlled ROS species—such as Cu–OOH or Cu=O intermediates—over unselective hydroxyl radicals, thus avoiding overoxidation and enhancing selectivity.

3.2.2. Gaining insight over the full catalytic wet peroxide oxidation (CWPO) reaction of DOP monitored by liquid HPLC

The overall multistep oxidation reaction of DOP to polydopamine is illustrated in Fig. 5a. Initially, DOP is oxidized to Dopamine-o-quinone (DQ) through a two-electron process. DQ then undergoes intramolecular cyclization to form leukoaminochrome (LAC), which is subsequently oxidized to aminochrome (AC). AC can rearrange into 5,6-dihydroxyindole (DHI), which is further oxidized to indole-5,6-quinone (IQ). The final products, DHI and IQ, can polymerize to form polydopamine through a complex series of condensation and oxidative couplings (Fig. 5a). The complete transformation of DOP was monitored using liquid chromatography. For this purpose, the same optimized conditions described in the previous section were applied, with the exception that 4-AP and sodium chloride were omitted from the reaction mixture.

The results obtained by liquid chromatography partially correlate with those obtained for BCM-3@Cu and BCM-4@Cu when monitoring the first step of the reaction (Fig. 5b-c). In particular, BCM-3@Cu exhibited slightly lower DOP conversion rates (Fig. 5b) compared to BCM-4@Cu (Fig. 5c), as evidenced by the concentration decrease of DOP in the reaction medium. It is worth noting that the data have not been normalized to the copper content; therefore, based on these results, BCM-4@Cu is expected to display higher TOF than BCM-3@Cu.

In contrast to the previous data, liquid chromatography indicates that BCM-5@Cu is the most efficient catalyst overall (Fig. 5d). DOP is fully converted within the first four hours of the reaction when using BCM-5@Cu compared to approximately 100 h required by its homologues. Of particular note is the fact that BCM-5@Cu has the highest copper content among the three, and that the data shown in the Fig. 5b-d have not been normalized in that respect. This mismatch with the results obtained from monitoring the first oxidation step by UV-Vis could be attributed to the strong overoxidation capacity of BCM-5@Cu. This property may drive the reaction rapidly beyond the formation of semiquinone or quinone intermediates—species that are essential for complex formation with 4-AP—thus reducing their

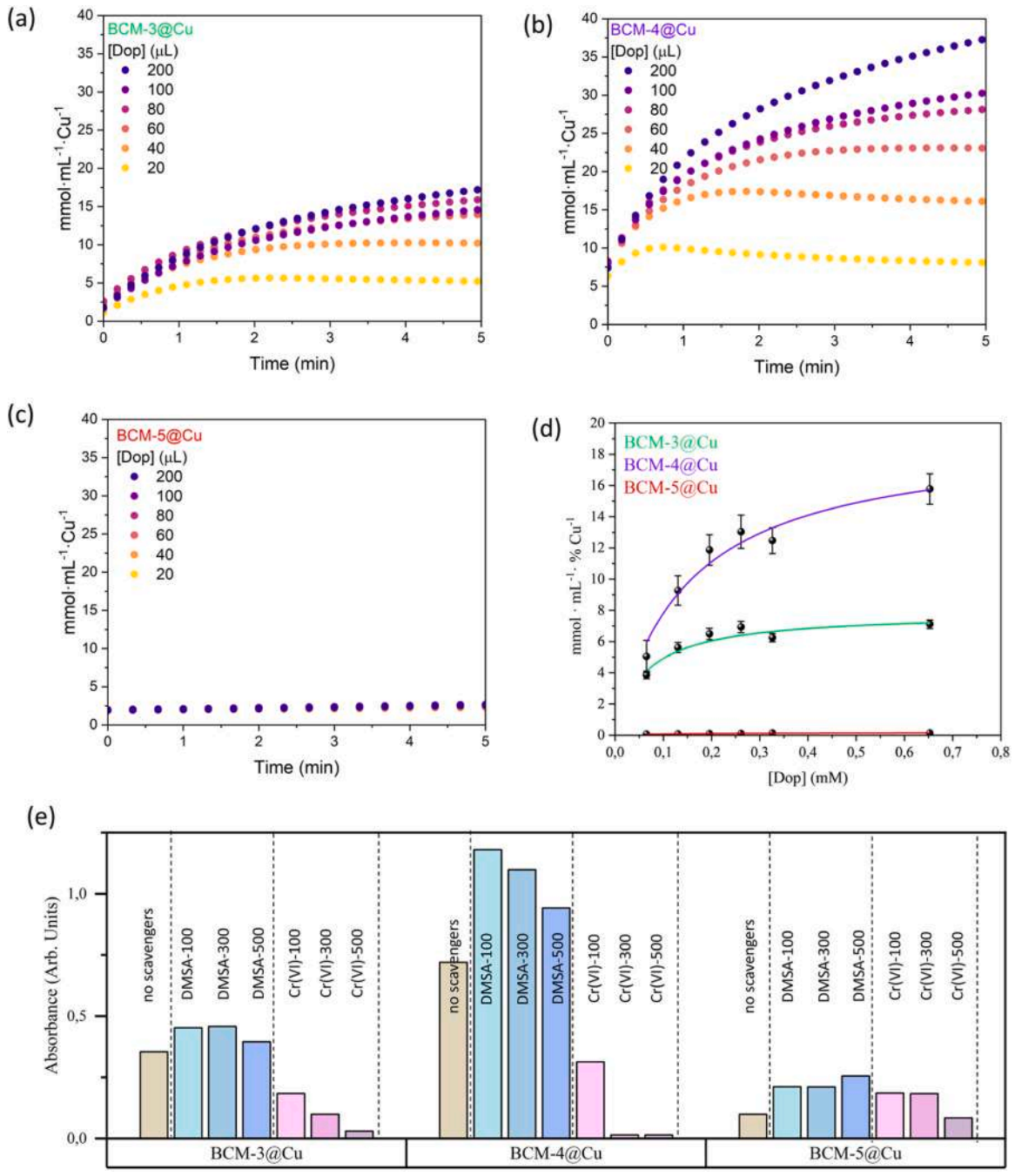

Fig. 4. Kinetics of DOP oxidation with different substrate concentrations for (a) BCM-3@Cu, (b) BCM-3@Cu and (c) BCM-4@Cu. The values of concentration of DOP oxidized have been normalized to the copper content of the catalysts after its exposition to hydrogen peroxide and dopamine solution. (d) Michaelis-Menten plot for the CWPO of DOP by BCM-3@Cu, BCM-4@Cu and BCM-5@Cu. (e) Absorbance after the dopamine oxidation in the presence of different concentrations of hydroxyl radicals (Dimethyl Sulfoxide – DMSO) and electron (hexavalent chromium – Cr(VI)) scavengers.

Table 2
- Summary of the V_{max} and K_M values extracted from the fittings of the Michaelis-Menten curves plot.

	K_M	V_{max}	R^2
BCM−3@Cu	0.06017 ± 0.01353	7.86458 ± 0.42068	0.92764
BCM−4@Cu	0.14685 ± 0.03258	19.25947 ± 1.53324	0.95625
BCM−5@Cu	0.16577 ± 0.06849	0.19282 ± 0.03398	0.8656

detectability by UV-Vis in the earlier assay.

Some intermediate products were identified by liquid chromatography, providing further insight into the mechanistic aspects of the DOP oxidation by our catalysts (insets of Fig. 5b–d). For BCM-3@Cu, 5,6-dihydroxyindole (DHI) was the only detectable intermediate. The concentration of DHI peaked at the beginning of the reaction and remained stable for approximately 24 h, after which it began to decline. This trend indicates that BCM-3@Cu is highly efficient in driving the complete oxidation of DOP to the final fully oxidized monomeric product (DHI), while its subsequent transformation into polydopamine appears to be a kinetically limited step that is not dependent on the presence of the catalyst [38,39]. Thus, although BCM-3@Cu shows slower DOP transformation kinetics in comparison to BCM-4@Cu and BCM-5@Cu —possibly due to a lower generation of oxidative species per mass of catalyst—it proves to be the most efficient in achieving complete DOP

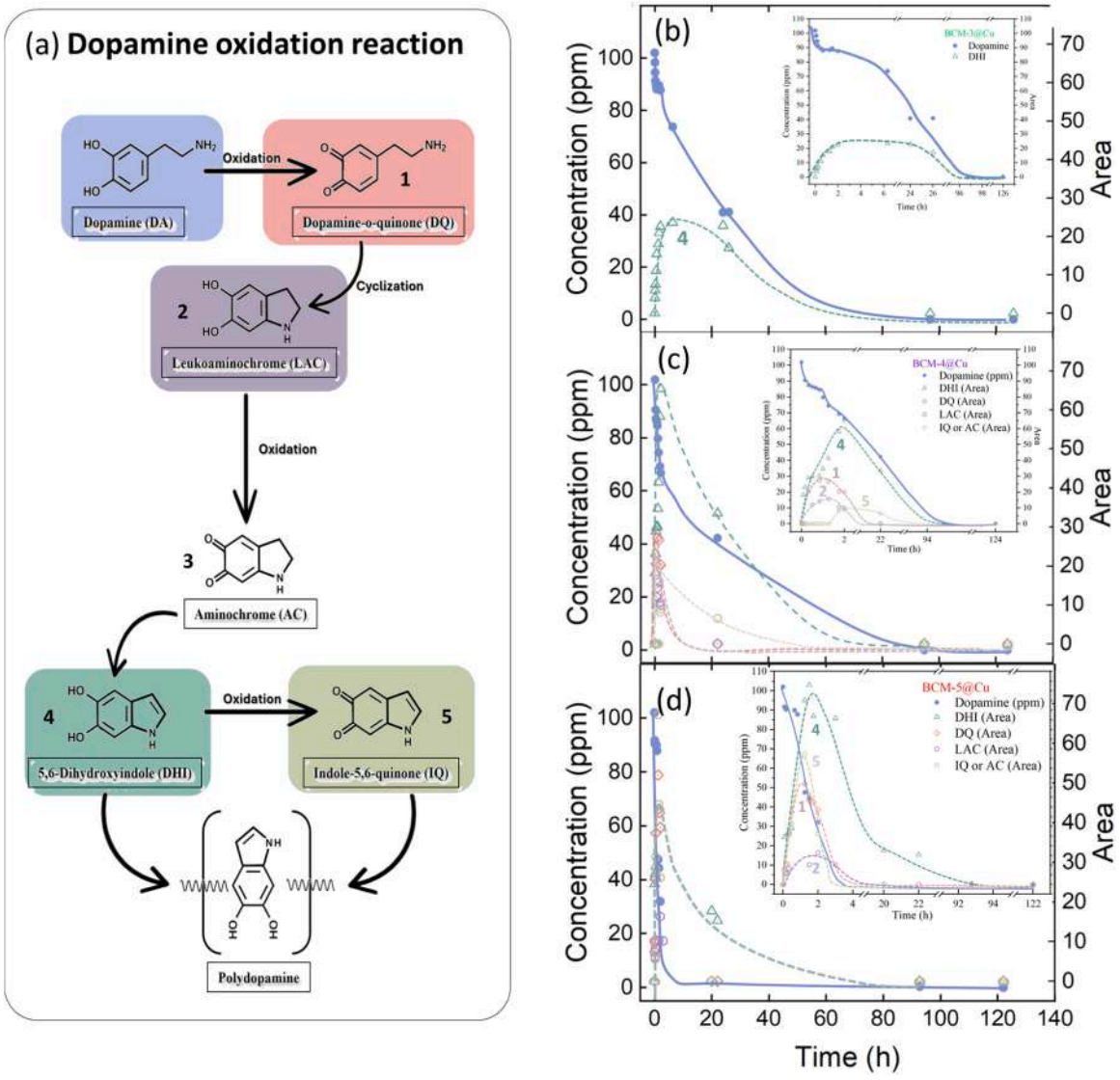

Fig. 5. (a) Full dopamine oxidation reaction identifying each of the key intermediate products. Dopamine oxidation reaction followed by HPLC for (b) BCM-3@Cu, (c) BCM-4@Cu and (d) BCM-5@Cu.

oxidation. This suggests that BCM-3@Cu effectively generates the appropriate oxidative species needed to drive the full reaction, without accumulating partially oxidized intermediates.

In contrast, for BCM-4@Cu and BCM-5@Cu, several early-stage intermediates were observed during the initial phase of the reaction. These species rapidly disappeared as the reaction progressed, giving rise to the formation of DHI and, to a lesser extent, IQ—the final oxidation products before polydopamine formation. Analyzing the time sequence of their appearance indicates that BCM-4@Cu and BCM-5@Cu promote the early formation of DQ and LAC together with DHI. DQ and LAC progressively disappeared giving rise to the formation of DHI and later in the reaction to IQ. This sequential formation of intermediates suggests an initial, intense but non-selective activation of hydrogen peroxide and the subsequent generation of ROS, which leads to dopamine oxidation. As the reaction progresses, this activity gradually shifts toward the oxidation of intermediate products into DHI, and subsequently to the formation of polydopamine [43]. Notably, BCM-5@Cu achieves a near-complete reduction of DOP concentration within the first four hours of the experiments, but that in parallel, is the catalysts that has the higher copper content from the studied in this work.

In the following step, the characteristics of the Cu sites installed in the C4-MOFs were thoroughly investigated to determine their local structure. This information is key to link structural aspects of the copper site to their catalytic performance.

3.3. Connecting the copper sites characteristics and their activity

A combination of UV-Vis, Electron Paramagnetic Resonance (EPR), and X-ray Absorption Spectroscopies (XAS) was employed to investigate the local structure of the copper sites in C4-MOFs. Copper loading was varied by exposing the MOFs to copper solutions of varying concentrations. In addition, the local structure of the copper sites under the catalytic conditions used for DOP oxidation was investigated ex situ by EPR spectroscopy.

Preliminarily, upon copper loading, BCM-3@Cu and BCM-4@Cu developed a pale blue colour, whereas BCM-5@Cu acquired a pale grey tone. Such differences in the color of the copper complexes stabilized in Zr-C4-MOFs qualitatively indicate that their electronic structure, which in turn is linked to their oxidation state and coordination environment, varies depending on the host material.

The UV-Vis spectra of BCM-3@Cu and BCM-4@Cu (Fig. 6a) show broad absorption bands, with maxima ranging from 710 to 800 nm for BCM-3@Cu and from 780 to 850 nm for BCM-4@Cu. These features are characteristic of the d–d electronic transitions of Cu(II) ions with a $3d^9$

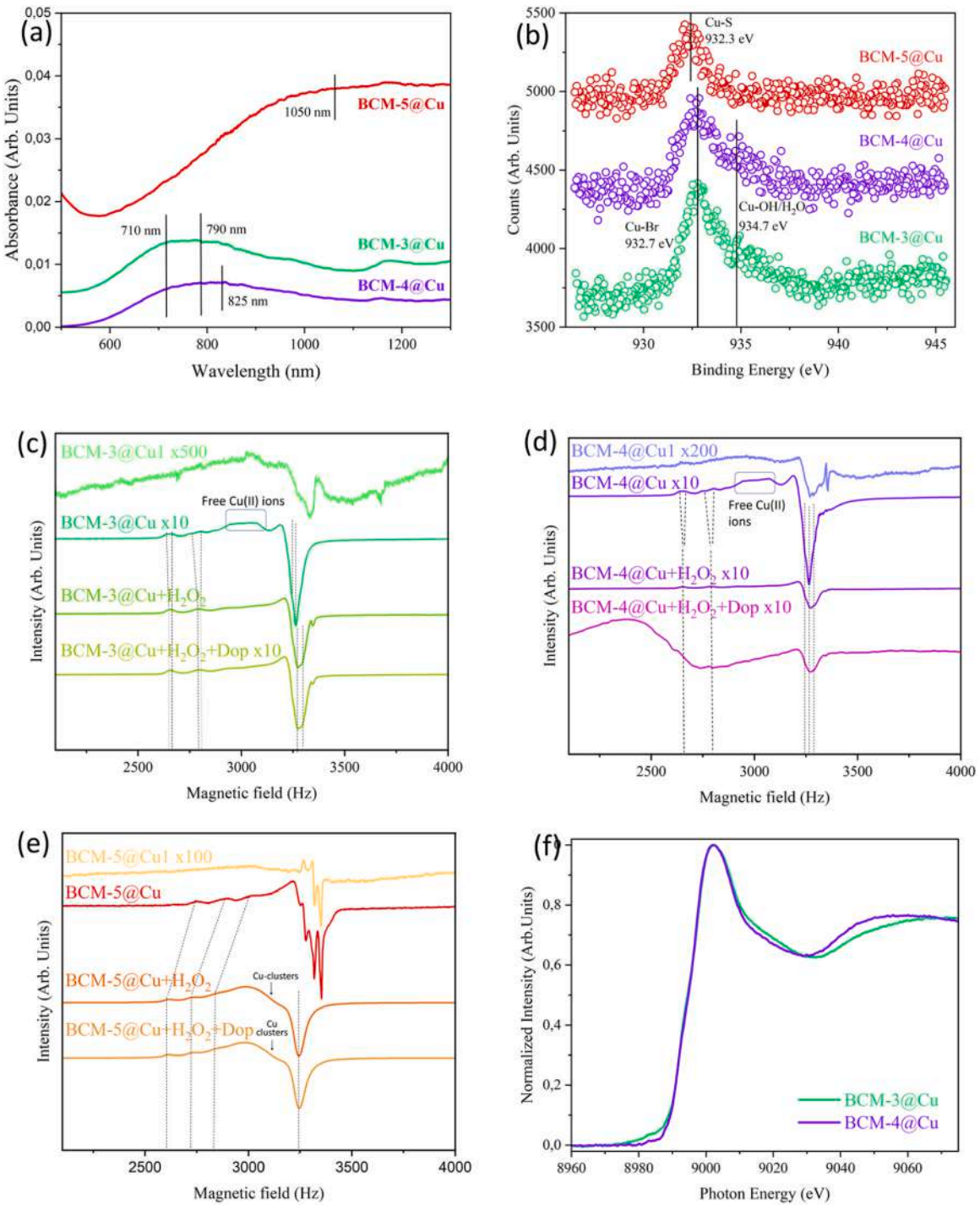

Fig. 6. (a) UV-Vis, (b) XPS and (c-e) X band EPR spectra of copper doped BCM-3@Cu, BCM-4@Cu and BCM-5@Cu compounds. (f) XAS spectra of BCM-3@Cu and BCM-4@Cu after exposure to H_2O_2.

configuration and differ slightly from the typical absorption of the $[Cu(H_2O)_6]^{2+}$ complex [61]. Interestingly, the observed red-shift is comparable to that reported for partially brominated CuBr and $CuBr_2$ complexes (e.g., 797 nm and 825 nm), suggesting a similar coordination environment for the copper ions stabilized within the frameworks of BCM-3@Cu and BCM-4@Cu [62–64].

When analyzing the UV-Vis spectra of BCM-5@Cu the signal becomes more complex, since the increase of the overall UV-Vis background suggests the co-existence of Cu(II) and partially reduced Cu(I)-thiolate species. This conclusion agrees with the UV-Vis spectra of Cu^{II}/ Cu^{I} mixed valence species found in many copper-thiolates having high background absorbances and broad absorption maxima located at much higher wavelength than the ones reported for Cu(II)-complexes [65,66].

XPS spectroscopy support the analysis obtained from UV-Vis spectroscopy (Fig. 6b). For BCM-3@Cu and BCM-4@Cu, the main signal, with a binding energy of 932.7 eV for Cu $2p_{3/2}$, matches with the formation of Cu-Br bonds after the metalation. A shoulder at higher binding energies (i.e. 933.7 eV) is as well detected and ascribed to the presence of Cu-H_2O moieties. The stabilization of at least a dual population of copper complex system into BCM-3@Cu and BCM-4@Cu agrees with the conclusions drawn by the UV-Vis spectroscopy. In comparison, BCM-

5@Cu shows only one peak with a slightly lower binding energy (932.4 eV) that agrees with the formation of Cu-S bonds in the structure.

X-band EPR spectra were measured to gain further detail on the copper speciation within our microporous frameworks (Fig. 6c-d). Again, the EPR signal of the copper ions depends mainly on the characteristics of the host materials, and thus, the profile of the EPR spectra of BCM-3@Cu and BCM-4@Cu differ significantly from the one obtained for BCM-5@Cu. BCM-3@Cu and BCM-4@Cu exhibit the characteristic EPR fingerprint of two magnetically isolated Cu(II) ions with slightly different tetragonal ligand field environments consisting of two central EPR absorption signal completed by four less intense maxima associated to their hyperfine structure lines. Both unique Cu ions are immobile, which indicate that they are likely coordinated to the Br anions arising from the bromosuccinic or the dibromosuccinic linkers of BCM-3@Cu and BCM-4@Cu [16,23]. Together with the UV-Vis data, EPR suggests that copper ions are immobilized as $Cu(H_2O)_5Br$ or $Cu(H_2O)_4Br_2$ species having elongated octahedral coordination environments. Further, the EPR data of both compounds exhibit a hump located approximately between 2950 and 3050 Hz in the X-band spectra, a signal that is usually associated to mobile copper species not anchored to the framework [23]. In fact, when the EPR spectra are recorded at low temperature, this contribution disappears because the mobile oxo-aquo cations are freeze. When BCM-3@Cu and BCM-4@Cu are exposed to the hydrogen peroxide solution employed for the DOP oxidation, the absorption signal associated with the copper hexa-aquo species disappears. This observation aligns with the decrease in copper content detected by X-ray fluorescence and indicates a homogenization of the coordination environments of the CuA and CuB species. Additionally, the EPR spectra of both BCM-3@Cu and BCM-4@Cu after their exposure to H_2O_2 are very similar, suggesting only minor changes in the coordination sphere of coper ions installed in both frameworks [67,68]. The EPR-signals after the exposure of BCM-3@Cu and BCM-4@Cu catalysts are consistent with octahedral Cu(II) ions situated in a tetragonal ligand field with slightly different g-values and hyperfine structures, a conclusion that aligns with the slight variations in bromination degree inferred from UV-Vis spectroscopy. In addition, the EPR spectra of the catalysts do not show any variation when the materials are further exposed to a DOP solution, suggesting that dopamine does not coordinate to the copper sites via its catechol ring. Thus, a direct electron-transfer reduction pathway can be ruled out in the case of the copper dopped BCM-3@Cu and BCM-4@Cu catalysts.

In contrast for BCM-3@Cu and BCM-4@Cu, the EPR signature of copper loaded BCM-5@Cu differs significantly from the ones obtained for the brominated frameworks. The initial spectra after the copper loading show a complex mixture of sharp signatures tentatively associated to a combination of thiol peroxyl, sulfonyl peroxyl and/or sulfinyl radicals. The intensity of this EPR lines increases with the copper loading of BCM-5@Cu, which matches with the redox-metal induced thiol-radicals generations reported in biologically relevant thiol or glutathione molecules [69–75]. Nevertheless, it is important to mention there that the formation and evolution of these Sulphur based organic radicals in thiol rich structures needs to be investigated in more detail to really uncover their formation mechanisms in thiol rich microporous MOF materials. Regarding the copper species, initially the copper signal is hidden by the spectral lines arising from Sulphur radicals, but once BCM-5@Cu is exposed to hydrogen peroxide and dopamine solutions, the organic radicals fully disappear and the dual contribution from copper ions can be observed in the material: (I) the signal of an isolated copper ion stabilized in a tetragonally distorted octahedral coordination, and (II) the presence of a broad signal centered At a $g_{\perp}$-value of 2.18 associated to copper clustered species close enough to stablish magnetic interactions. The $g_{\perp}/g_{\parallel}$ values and the hyperfine splitting of the copper isolated sites stabilized in BCM-5 ($(g_{\perp} = 2.12, g_{\parallel} = 2.43, A_{\parallel} = 130 \times 10^{-4}$) slightly differ from the ones observed in BCM-3@Cu and BCM-4@Cu ($g_{\perp} = 2.09$, $g_{\parallel} = 2.38$–2.36, $A_{\parallel} = 124$–123×10^{-4}), but still all of them lie within the usual values observed for CuO_6 octahedral complexes. All in all, considering the UV-Vis and EPR data, the copper ions are preferentially stabilized in elongated octahedral coordination environments, with Br and S atoms occupying one or two of the axial positions.

Last but not least, the copper-loaded samples BCM-3@Cu and BCM-4@Cu, after exposure to the H_2O_2 solution used for DOP oxidation, were analysed by X-ray absorption spectroscopy (XAS) at the Cu *K*-edge in total fluorescence yield mode. The absorption edge for both

BCM-3@Cu and BCM-4@Cu appears near 9000 eV, and the absence of the characteristic pre-edge feature around 8980 eV confirms that the copper ions are predominantly in the Cu(II) oxidation state. Both spectra also exhibit a shoulder at slightly lower energies than the main edge and a second feature around 9015 eV. These features are consistent with those observed in oxygen-rich Cu(II) environments, such as CuO, $Cu(OH)_2$, or Cu(II) ions stabilized in zeolite matrices [76].

The most notable—and subtle—difference between the spectra of BCM-3@Cu and BCM-4@Cu lies in the high-energy region: the maximum of the final feature is located at approximately 9050 eV in BCM-4@Cu, shifting to about 9065 eV in BCM-3@Cu. These small variations in the absorbance of the second post-edge feature, along with slight differences in the energy position of the last absorption maxima, suggest subtle changes in the local coordination environment of the copper ions. This may reflect variations in the degree of partial bromination of the copper centres, as also indicated by EPR and UV-Vis spectroscopy.

When combining the structural features of BCM-3@Cu, BCM-4@Cu and BCM-5@Cu with the spectroscopic information arising from UV-Vis, XPS and EPR techniques, local structural models for the copper ions stabilized within the frameworks, and a tentative mechanism for the DOP oxidation, can be proposed (Fig. 7).

It is important to review at this point, that the oxidative steps of the DOP reaction can proceed via different reaction paths. First, it is well known that the copper complexation by catechol increases the electrophilicity of the copper-center, favoring the electron transfer from the ring and in parallel triggering the Cu(II) to Cu(I) reduction. Once the first electron transfer reaction has occurred, hydrogen peroxide would regenerate the Cu(I) to Cu(II) giving rise to the formation of additional hydroxyl radicals that could fasten even more the DOP oxidation (Eqs. (2)–(3)). Nevertheless, this reaction pathway is discarded since the EPR ruled out any variation on the coordination of the copper ions when the catalyst is exposed to dopamine [38,40].

$$Cu^{2+}\text{catechol} \rightarrow Cu^{+} + \text{semiquinone} \quad (2)$$

$$Cu^{2+}\text{semiquinone} \rightarrow Cu^{+} + \text{quinone} \quad (3)$$

$$Cu^{+} + H_2O_2 \rightarrow Cu^{2+} + OH^{-} + \cdot OH \quad (4)$$

As a second mechanisms of reaction, the direct activation of the hydrogen peroxide by Cu(II) can give rise to the formation of copper-hydroperoxo complexes, which can undergo inner-sphere electron transfer or directly oxidize the target substrate (*i.e. especially phenols or catechols*) (Eq. (5)),

$$Cu^{2+} + H_2O_2 \rightarrow \left[Cu^{2+} - OOH\right] + H^{+} \quad (5)$$

Last, but not least, hydrogen peroxide can as well induce the Cu(II) → Cu(I) reduction (Eq. (6)), generating hydroperoxide radicals. Cu(I) centers can re-enter into the Fenton cycle via Eq. (4), generating additional hydroxyl groups that can take part directly in the oxidation of DOP to quinones, as well as in the following oxidative steps towards the DOP transformation into polydopamine.

$$Cu^{2+} + H_2O_2 \rightarrow Cu^{+} + \cdot OOH + H^{+} \quad (6)$$

Taking this background information into account, BCM-3@Cu and BCM-4@Cu represent the easier cases of study to elucidate the DOP

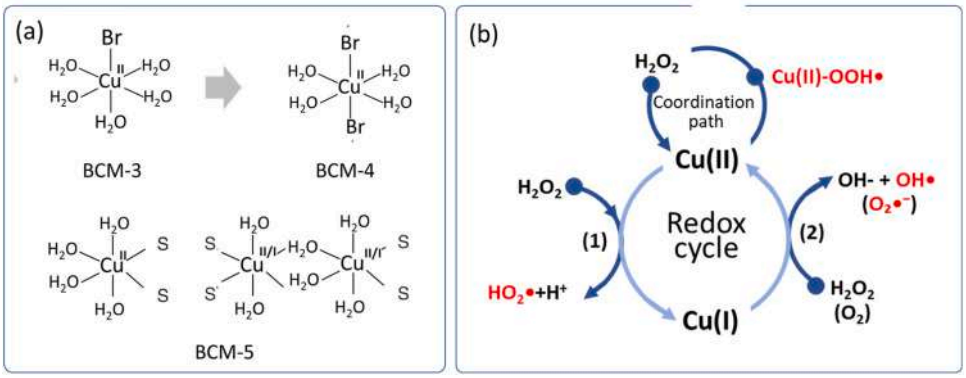

Fig. 7. Illustration of: (i) the tentative coordination environments proposed for the copper species stabilized in C4-MOFs, and (b) the possible reaction paths identified in the copper catalysts studied in this work.

oxidation mechanisms in these brominated rich frameworks stabilizing copper sites. When comparing both catalysts, BCM-3@Cu presents a relatively open framework, with bromosuccinic linkers highly diluted within the structure and a lower concentration of HBr in the pore space compared to BCM-4@Cu. Those characteristics makes copper ions to be stabilized mainly as copper-aquo complexes with one of their apical positions occupied by one of the bromide anions belonging to the bromosuccinate organic linkers. In contrast to BCM-3@Cu, BCM-4@Cu exhibit a tetragonal structure with a higher density of bromine groups decorating a smaller pore space. In addition, the content of free bromidic acid molecules encapsulated within the pore space is higher in BCM-4@Cu than in BCM-3@Cu. These structural features increase the likelihood of copper ions being stabilized as copper aquo complexes with two bromide anions forming part of their coordination environment. Although this difference is subtle, it has a significant impact on the electronic structure of the copper ions, ultimately influencing their catalytic activity (Fig. 7a). When analyzing the possible coordination modes of copper in BCM-5@Cu, a more complex scenario emerges. In addition to isolated copper aquo species—where apical positions in the coordination environment are partially replaced by S^- anions belonging to dimercaptosussinate linkers, UV-Vis and EPR spectral features also suggest the formation of copper clusters and the coexistence of mixed-valence copper species. Therefore, BCM-5@Cu will be set aside from the current discussion and revisited later after analysing the DOP oxidation by BCM-3@Cu and BCM-4@Cu (Fig. 7b).

Thus, in summary, three main factors differentiate BCM-3@Cu from BCM-4@Cu: (i) BCM-4@Cu has a narrower pore structure, (ii) it contains a lower overall copper content, and (iii) the copper sites in BCM-4@Cu are more extensively coordinated by bromide ions. Dicarded the DOP transformation involving its direct coordination to the copper centers, its oxidation may be driven by the generation of: (I) Peroxyhydroxyl radical species -both coordinated to the copper centers (Fig. 7b(3)) or generated during the hydrogen peroxide activation by the Cu(II) to Cu(I) reduction (Fig. 7b(1)); or (II) the hydroxyl radicals generated during the hydrogen peroxide activation by Cu(I) to Cu(II) oxidation (Fig. 7b(2)). Although the formation of copper-coordinated peroxyhydroxyl radicals cannot be entirely excluded as a secondary pathway in the oxidation of DOP, the redox cycling of copper ions appears to be the dominant mechanism during the initial stages of DOP transformation. This conclusion is supported by the pronounced suppression of catalytic activity observed upon the addition of electron scavengers, such as hexavalent chromium (see Fig. 4e for details). Conversely, the introduction of dimethyl sulfoxide (DMSO), a known hydroxyl radical scavenger, results in a slight yet unexpected enhancement of the catalytic activity, particularly in the case of BCM-4@Cu. If hydroxyl radicals were the primary oxidants, their scavenging would be expected to inhibit the reaction. This counterintuitive observation may suggest that peroxyhydroxyl radicals exhibit a higher selectivity toward the initial oxidation step of DOP to DQ. This hypothesis is consistent with the reported reactivity profiles of catecholamines toward reactive oxygen species, where DOP displays high scavenging efficiency for superoxide and singlet oxygen, but relatively low reactivity toward hydroxyl radicals and their analogues [77,78]. As previously discussed, analogous trends have been reported wherein the activation pathway of hydrogen peroxide (H_2O_2) shifts to favor the formation of more controlled reactive oxygen species (ROS), such as copper–hydroperoxo (Cu–OOH) or copper–oxo (Cu═O) intermediates, over unselective hydroxyl radicals. This shift mitigates overoxidation and enhances catalytic selectivity. For instance, Kim et al. demonstrated that a Cu(II)–OOH intermediate undergoes homolytic cleavage, leading to site-specific oxidation reactions, thereby avoiding the indiscriminate reactivity associated with free hydroxyl radicals [79]. As derived from the results of the catalytic reaction followed by the colorimetric protocol, the inclusion of bromide anions in the coordination sphere of the copper ions makes the individual catalytic sites more efficient for the first DOP oxidation step; partially mirror the trends observed for DOP disappearance as monitored by liquid chromatography. The main different in this second experiment is the generation of intermediate reactive species in between DOP and polydopamine by BCM-3@Cu and BCM-4@Cu. Although the selectivity of the Cu-site could have an important influence here, the narrow pore space of BCM-4@Cu (and BCM-5@Cu) can add some diffusion constrains to the reaction, leading to the stabilization of intermediate products that are not observed in the case of BCM-3@Cu. To conclude, in addition to the kinetic limitations also observed for the BCM-5@Cu catalyst, the presence of mixed-valence Cu (II)/Cu(I) species in BCM-5@Cu may contribute to a more pronounced generation of reactive oxygen species (ROS) from both sides of the redox couple at the very onset of the reaction. In this particular case, establishing a direct correlation between catalytic activity and the nature of the metal sites is challenging, owing to the coexistence of multiple copper species within the framework and the significantly different copper content compared to BCM-3@Cu and BCM-4@Cu. Nevertheless, in general terms, copper sites coordinated by bromide and thiolate (S-based) ligands exhibit substantially higher catalytic activity than those in copper-doped MOF-801, where the coordination environment of copper is limited exclusively to oxygen donor atoms. This conclusion aligns with the modulation of both the electronic structure and redox properties of copper centers coordinated by softer donor ligands such as Br^- and S^{2-}. Their presence in the coordination sphere lowers the Cu (II)/Cu(I) redox potential, thereby facilitating redox cycling, and the subsequent ROS generation [80,81].

4. Conclusion

The assembly of three new microporous Metal-Organic Frameworks from bromosuccinic, dibromosuccinic and dimercaptosuccinic C4-

organic linkers have allowed the stabilization of copper ions with halogen rich coordination environments into their pore space. Depending on the organic linker employed in the synthesis, the materials are stabilized in an open cubic framework, or an axially compressed tetragonal structure, both exhibiting with the typical "fcu" topology of the twelve connected Zr(IV)-MOFs. Although the synthesis conditions induce a significant debromination of the bromosuccinic and dibromosuccinic acids, the bromide anions released from the linkers are partially trapped within the pore space of the microporous frameworks. All in all, the structural features of the halogen rich microporous Zr-C4-MOFs enable the stabilization of copper ions with a bromide and Sulphur rich coordination environments under reaction conditions. The catalytic activity to oxidize dopamine substrate via the activation of hydrogen peroxide is greatly influenced by the features of the coordination environment of the copper sites. In fact, the integration of bromide anions into the coordination sphere of isolated copper centers promotes significantly the activity of the catalysts when compared in terms of turn over frequency per metal site.

Although copper catalysts stabilized via thiolate-based organic linkers initially appeared inactive when evaluated by colorimetric assays, they were ultimately revealed to be the most efficient catalysts when DOP oxidation was monitored using liquid chromatography. Notably, the catalysts with narrower pore structures (BCM-4@Cu and BCM-5@Cu) demonstrated a higher tendency to retain intermediate species of the DOP oxidation pathway, indicating possible kinetic limitations in product release or transformation.

Crucially, the incorporation of bromide and thiolate (Br/S) groups into the coordination sphere of the copper centres emerged as a key factor for catalytic performance. In contrast, copper-doped MOF-801—where copper is coordinated exclusively by oxygen atoms—displayed negligible activity, highlighting the importance of the ligand environment.

Taken together with the results obtained in the presence of reactive oxygen species scavengers, the data strongly suggest that the Br/S-containing coordination environment modulates the electronic structure of the copper ions, lowering the Cu(II)/Cu(I) redox potential. This promotes efficient redox cycling, enhances redox flexibility, and favours the generation of more selective ROS intermediates. These effects ultimately contribute to improved catalytic efficiency and selectivity in the oxidation of DOP.

Overall, this study demonstrates how halide-rich copper centers can be stabilized within ad-hoc designed microporous MOFs, and their catalytic activity to activate hydrogen peroxide and oxidase DOP altered depending on the characteristics of their coordination environment. In fact, the control of the debromination process by softening the synthesis conditions could open the room to the future design of Zr-C4-MOFs with higher halide concentrations in their frameworks, and hence, in the metal centers installed within their pore space. By modulating the redox properties of the copper sites and their ability to selectively generate reactive oxygen species (ROS), these catalysts not only offer a pathway to better control DOP oxidation for the tailored formation of polydopamine films, but also open the room to the application of brominated/thiolated copper-based systems in the broader field of copper redox catalysis, as widely reported in the literature.

CRediT authorship contribution statement

Miryam Gil-Calvo: Writing – review & editing, Supervision, Project administration, Methodology, Investigation, Formal analysis, Conceptualization. **Roberto Fernández de Luis:** Writing – review & editing, Writing – original draft, Visualization, Supervision, Project administration, Funding acquisition, Data curation, Conceptualization. **E. Vidal-Martin:** Writing – review & editing, Writing – original draft, Methodology, Investigation, Formal analysis, Data curation. **Itziar Oyarzabal:** Writing – review & editing, Project administration, Funding acquisition, Data curation. **A. Rogalev:** Investigation, Data curation. **M. Calles García:** Writing – review & editing, Writing – original draft, Visualization, Methodology, Investigation, Formal analysis, Data curation. **Pedro Luis Arias:** Writing – review & editing, Supervision, Project administration, Formal analysis, Conceptualization. **Jorge Sáiz:** Writing – review & editing, Methodology, Investigation, Formal analysis, Data curation. **Viktor Petrenko:** Writing – review & editing, Visualization, Supervision, Funding acquisition, Formal analysis, Data curation. **N.J. Yutronkie:** Investigation, Data curation. **Iker Agirrezabal-Tellería:** Writing – review & editing, Supervision, Project administration, Funding acquisition, Formal analysis, Conceptualization.

Declaration of Competing Interest

The authors declare that they have no known competing financial interests or personal relationships that could have appeared to influence the work reported in this paper.

Acknowledgements

The authors thank the financial support as well from the Spanish Agencia Estatal de Investigación, (AEI) through EVOLMOF PID2021–122940OB-C31 and CAPSOLBVE (AEI/FEDER, UE) PID2021–122940OB-C33 (including FEDER financial support), ENZY-MOF (TED2021–130621B-C42) and Tailing23Green-ERAMIN projects. This study was funded as well by the Basque Government IKUR Program and Industry and Education Departments under the ELKARTEK (SMYRNA) and PIBA (PIBA-2022–1–0032) programs. The HORIZON-MSCA-2022-SE-01–01 SELFAQUASENS (101131379) which received funding from the Horizon Europe Research and Innovation Programme, is also acknowledged. This research was supported through 4AirCRAFT project under the strategic international cooperation between Europe (Horizon2020, No.101022633) and Japan Science and Technology Agency (JST) with reference number JPMJSC2102. Elvira Vidal thanks the Basque Government (Education Department) for her PhD grant (PRE_2024_1_0283). The authors thank the technical and human support provided by SGIker (UPV/EHU).

Appendix A. Supporting information

Supplementary data associated with this article can be found in the online version at doi;10.1016/j.cattod.2025.115484

Data availability

Data will be made available on request.

References

[1] C.E. Elwell, N.L. Gagnon, B.D. Neisen, D. Dhar, A.D. Spaeth, G.M. Yee, W. B. Tolman, Copper-oxygen complexes revisited: structures, spectroscopy, and reactivity, Chem. Rev. 117 (2017) 2059–2107, https://doi.org/10.1021/ACS.CHEMREV.6B00636/ASSET/IMAGES/MEDIUM/CR-2016-00636B_0043.GIF.

[2] R. Trammell, K. Rajabimoghadam, I. Garcia-Bosch, Copper-promoted functionalization of organic molecules: from biologically relevant Cu/O 2 model systems to organometallic transformations, Chem. Rev. 119 (2019) 2954–3031, https://doi.org/10.1021/ACS.CHEMREV.8B00368.

[3] M. Fontecave, J.L. Pierre, Oxidations by copper metalloenzymes and some biomimetic approaches, Coord. Chem. Rev. 170 (1998) 125–140, https://doi.org/10.1016/S0010-8545(98)00068-X.

[4] Y. Sun, P. Tian, D. Ding, Z. Yang, W. Wang, H. Xin, J. Xu, Y.F. Han, Revealing the active species of Cu-based catalysts for heterogeneous Fenton reaction, Appl. Catal. B 258 (2019), https://doi.org/10.1016/j.apcatb.2019.117985.

[5] zsef Balla, la Tamis Kiss, R.F. Jamesonlb, 1992, Copper(11)-Catalyzed Oxidation of Catechol by Molecular Oxygen in Aqueous Solution.

[6] M. Fontecave, J.L. Pierre, Oxidations by copper metalloenzymes and some biomimetic approaches, Coord. Chem. Rev. 170 (1998) 125–140, https://doi.org/10.1016/S0010-8545(98)00068-X.

[7] K.A. Lomachenko, A. Martini, D.K. Pappas, C. Negri, M. Dyballa, G. Berlier, S. Bordiga, C. Lamberti, U. Olsbye, S. Svelle, P. Beato, E. Borfecchia, The impact of reaction conditions and material composition on the stepwise methane to methanol

conversion over Cu-MOR: An operando XAS study, Catal. Today 336 (2019) 99–108, https://doi.org/10.1016/j.cattod.2019.01.040.
[8] J. Wang, Q. Wa, Q. Diao, F. Liu, F. Hao, Y. Xiong, Y. Wang, J. Zhou, X. Meng, L. Guo, Z. Fan, Atomic design of copper active sites in pristine metal–organic coordination compounds for electrocatalytic carbon dioxide reduction, Small Methods 8 (2024) 2400432, https://doi.org/10.1002/smtd.202400432.
[9] Y. Zhang, Q. Zhou, Z.-F. Qiu, X.-Y. Zhang, J.-Q. Chen, Y. Zhao, F. Gong, W.-Y. Sun, Tailoring coordination microenvironment of Cu(I) in metal–organic frameworks for enhancing electroreduction of CO2 to CH4, Adv. Funct. Mater. 32 (2022) 2203677, https://doi.org/10.1002/adfm.202203677.
[10] Y.-Y. Liu, H.-L. Zhu, Z.-H. Zhao, N.-Y. Huang, P.-Q. Liao, X.-M. Chen, Insight into the effect of the d-orbital energy of copper ions in metal–organic frameworks on the selectivity of electroreduction of CO2 to CH4, ACS Catal. 12 (2022) 2749–2755, https://doi.org/10.1021/acscatal.1c04805.
[11] P.J. Deuss, R. Denheeten, W. Laan, P.C.J. Kamer, Bioinspired catalyst design and artificial metalloenzymes, Chem. A Eur. J. 17 (2011) 4680–4698, https://doi.org/10.1002/CHEM.201003646.
[12] H. Eom, W.J. Song, Emergence of metal selectivity and promiscuity in metalloenzymes, J. Biol. Inorg. Chem. 24 (2019) 517–531, https://doi.org/10.1007/s00775-019-01667-0.
[13] E.N. Mirts, A. Bhagi-Damodaran, Y. Lu, Understanding and modulating metalloenzymes with unnatural amino acids, non-native metal ions, and non-native metallocofactors, Acc. Chem. Res 52 (2019) 935–944, https://doi.org/10.1021/ACS.ACCOUNTS.9B00011.
[14] Y.-W. Lin, Rational design of metalloenzymes: from single to multiple active sites, Coord. Chem. Rev. 336 (2017) 1–27, https://doi.org/10.1016/j.ccr.2017.01.001.
[15] Y. Yu, X. Liu, J. Wang, Expansion of redox chemistry in designer metalloenzymes, Acc. Chem. Res 52 (2019) 557–565, https://doi.org/10.1021/acs.accounts.8b00627.
[16] L. Gala, M. Lawson, K. Jomova, L. Zelenicky, A. Congradyova, M. Mazur, M. Valko, EPR spectroscopy of a clinically active (1:2) Copper(II)-histidine complex used in the treatment of menkes disease: a fourier transform analysis of a fluid CW-EPR spectrum, Molecules 19 (2014), https://doi.org/10.3390/molecules19010980.
[17] P. Chaudhuri, M. Hess, J. Müller, K. Hildenbrand, E. Bill, T. Weyhermüller, K. Wieghardt, Aerobic oxidation of primary alcohols (including methanol) by copper(II)- and zinc(N)-phenoxyl radical catalysts, J. Am. Chem. Soc. 121 (1999) 9599–9610, https://doi.org/10.1021/JA991481T.
[18] M. Perfecto-Irigaray, I. Merino-Garcia, J. Albo, G. Beobide, O. Castillo, A. Luque, S. Pérez-Yáñez, Copper(II)-porphyrin functionalized titanium(IV) metal-organic aerogels for the visible-light driven conversion of CO2 to alcohols, Mater. Today Energy 36 (2023) 101346, https://doi.org/10.1016/j.mtener.2023.101346.
[19] V. Mahadevan, R.K. Gebbink, T.D. Stack, Biomimetic modeling of copper oxidase reactivity, Curr. Opin. Chem. Biol. 4 (2000) 228–234.
[20] M. Albert-Soriano, I.M. Pastor, Metal–organic framework based on copper and carboxylate-imidazole as robust and effective catalyst in the oxidative amidation of carboxylic acids and formamides, Eur. J. Org. Chem. 2016 (2016) 5180–5188, https://doi.org/10.1002/ejoc.201600991.
[21] K.T. Dinh, M.M. Sullivan, K. Narsimhan, P. Serna, R.J. Meyer, M. Dincă, Y. Román-Leshkov, Continuous partial oxidation of methane to methanol catalyzed by diffusion-paired copper dimers in copper-exchanged zeolites, J. Am. Chem. Soc. 141 (2019) 11641–11650, https://doi.org/10.1021/jacs.9b04906.
[22] B.E.R. Snyder, M.L. Bols, R.A. Schoonheydt, B.F. Sels, E.I. Solomon, Iron and copper active sites in zeolites and their correlation to metalloenzymes, Chem. Rev. 118 (2018) 2718–2768, https://doi.org/10.1021/ACS.CHEMREV.7B00344/ASSET/IMAGES/MEDIUM/CR-2017-00344F_0069.GIF.
[23] P.C. Bruzzese, E. Salvadori, S. Jäger, M. Hartmann, B. Civalleri, A. Pöppl, M. Chiesa, 17O-EPR determination of the structure and dynamics of copper single-metal sites in zeolites, Nat. Commun. 12 (2021), https://doi.org/10.1038/s41467-021-24935-7.
[24] M. Zhao, S. Ou, C.De Wu, Porous metal-organic frameworks for heterogeneous biomimetic catalysis, Acc. Chem. Res 47 (2014) 1199–1207, https://doi.org/10.1021/AR400265X/ASSET/IMAGES/LARGE/AR-2013-00265X_0010.JPEG.
[25] Y. Bai, Y. Dou, L.H. Xie, W. Rutledge, J.R. Li, H.C. Zhou, Zr-based metal-organic frameworks: design, synthesis, structure, and applications, Chem. Soc. Rev. 45 (2016) 2327–2367, https://doi.org/10.1039/c5cs00837a.
[26] M. Viciano-Chumillas, X. Liu, A. Leyva-Pérez, D. Armentano, J. Ferrando-Soria, E. Pardo, Mixed component metal-organic frameworks: Heterogeneity and complexity at the service of application performances, Coord. Chem. Rev. 451 (2022) 214273, https://doi.org/10.1016/J.CCR.2021.214273.
[27] S. Øien-ØDegaard, B. Bouchevreau, K. Hylland, L. Wu, R. Blom, C. Grande, U. Olsbye, M. Tilset, K.P. Lillerud, UiO-67-type metal-organic frameworks with enhanced water stability and methane adsorption capacity, Inorg. Chem. 55 (2016) 1986–1991, https://doi.org/10.1021/acs.inorgchem.5b02257.
[28] A. Valverde, G.I. Tovar, N.A. Rio-López, D. Torres, M. Rosales, S. Wuttke, A. Fidalgo-Marijuan, J.M. Porro, M. Jiménez-Ruiz, V. García Sakai, A. García, J. M. Laza, J.L. Vilas-Vilela, L. Lezama, M.I. Arriortua, G.J. Copello, R. Fernández De Luis, Designing metal-chelator-like traps by encoding amino acids in zirconium-based metal-organic frameworks, Chem. Mater. (2022), https://doi.org/10.1021/ACS.CHEMMATER.2C02431/SUPPL_FILE/CM2C02431_SI_001.PDF.
[29] G. Zan, Q. Wu, G. Zan, Q. Wu, Biomimetic and bioinspired synthesis of nanomaterials/nanostructures, Adv. Mater. 28 (2016) 2099–2147, https://doi.org/10.1002/ADMA.201503215.
[30] J. Baek, B. Rungtaweevoranit, X. Pei, M. Park, S.C. Fakra, Y.S. Liu, R. Matheu, S. A. Alshmimri, S. Alshehri, C.A. Trickett, G.A. Somorjai, O.M. Yaghi, Bioinspired metal-organic framework catalysts for selective methane oxidation to methanol, J. Am. Chem. Soc. 140 (2018) 18208–18216, https://doi.org/10.1021/jacs.8b11525.
[31] A. Valverde, E. Alkain, N.A. Rio-López, L. Lezama, A. Fidalgo-Marijuan, J.M. Laza, S. Wuttke, J.M. Porro, I. Oyarzabal, M. Jiménez-Ruiz, V. García Sakai, P.L. Arias, I. Agirrezabal-Telleria, R. Fernández de Luis, Enzyme-mimicking of copper-sites in metal–organic frameworks for oxidative degradation of phenolic compounds, J. Mater. Chem. A Mater. 12 (2024) 4555–4571, https://doi.org/10.1039/D3TA06198A.
[32] A. Moghaddasfar, G. Mohammadi Ziarani, R. Luque, A. Badiei, Unveiling the synergy between plasma and metal–organic frameworks for next-generation materials: an overview, Mater. Adv. 6 (2025) 3416–3432, https://doi.org/10.1039/D5MA00171D.
[33] Y. Wu, W. Zhao, S.H. Ahn, Y. Wang, E.D. Walter, Y. Chen, M.A. Derewinski, N. M. Washton, K.G. Rappé, Y. Wang, D. Mei, S.B. Hong, F. Gao, Interplay between copper redox and transfer and support acidity and topology in low temperature NH3-SCR, Nat. Commun. 14 (2023), https://doi.org/10.1038/s41467-023-38309-8.
[34] D. La Mendola, G. Arena, A. Pietropaolo, C. Satriano, E. Rizzarelli, Metal ion coordination in peptide fragments of neurotrophins: a crucial step for understanding the role and signaling of these proteins in the brain, Coord. Chem. Rev. 435 (2021) 213790, https://doi.org/10.1016/j.ccr.2021.213790.
[35] M. Aghajani Hashjin, S. Zarshad, H.B. Motejadded Emrooz, S. Sadeghzadeh, Enhanced atmospheric water harvesting efficiency through green-synthesized MOF-801: a comparative study with solvothermal synthesis, Sci. Rep. 13 (2023) 16983, https://doi.org/10.1038/s41598-023-44367-1.
[36] H. Furukawa, F. Gándara, Y.B. Zhang, J. Jiang, W.L. Queen, M.R. Hudson, O. M. Yaghi, Water adsorption in porous metal-organic frameworks and related materials, J. Am. Chem. Soc. 136 (2014) 4369–4381, https://doi.org/10.1021/ja500330a.
[37] S. Wang, M. Wahiduzzaman, L. Davis, A. Tissot, W. Shepard, J. Marrot, C. Martineau-Corcos, D. Hamdane, G. Maurin, S. Devautour-Vinot, C. Serre, A robust zirconium amino acid metal-organic framework for proton conduction, Nat. Commun. 9 (2018) 4937, https://doi.org/10.1038/s41467-018-07414-4.
[38] M. Bisaglia, S. Mammi, L. Bubacco, Kinetic and structural analysis of the early oxidation products of dopamine: analysis of the interactions with α-synuclein, J. Biol. Chem. 282 (2007) 15597–15605, https://doi.org/10.1074/jbc.M610893200.
[39] M. Ravera, E. Gabano, Role of metal ions in dopamine oxidation, J. Chem. Educ. 98 (2021) 4031–4036, https://doi.org/10.1021/acs.jchemed.1c00744.
[40] A.N. Pham, T.D. Waite, Cu(II)-catalyzed oxidation of dopamine in aqueous solutions: Mechanism and kinetics, J. Inorg. Biochem 137 (2014) 74–84, https://doi.org/10.1016/j.jinorgbio.2014.03.018.
[41] M. Al-waeel, J. Lukkari, H. Kivelä, M. Salomäki, Heterogenous copper(0)-assisted dopamine oxidation: a new pathway to controllable and scalable polydopamine synthesis, Langmuir 40 (2024) 20133–20148, https://doi.org/10.1021/acs.langmuir.4c02460.
[42] S. Ito, A. Napolitano, T. Sarna, K. Wakamatsu, Iron and copper ions accelerate and modify dopamine oxidation to eumelanin: implications for neuromelanin genesis, J. Neural Transm. 130 (2023) 29–42, https://doi.org/10.1007/s00702-022-02574-6.
[43] W. Cheng, X. Zeng, H. Chen, Z. Li, W. Zeng, L. Mei, Y. Zhao, Versatile polydopamine platforms: synthesis and promising applications for surface modification and advanced nanomedicine, ACS Nano 13 (2019) 8537–8565, https://doi.org/10.1021/acsnano.9b04436.
[44] Z. Rao, K. Feng, B. Tang, P. Wu, Surface decoration of amino-functionalized metal-organic framework/graphene oxide composite onto polydopamine-coated membrane substrate for highly efficient heavy metal removal, ACS Appl. Mater. Interfaces 9 (2017) 2594–2605, https://doi.org/10.1021/acsami.6b15873.
[45] S. El Yakhlifi, M.-L. Alfieri, Y. Arntz, M. Eredia, A. Ciesielski, P. Samorì, M. d'Ischia, V. Ball, Oxidant-dependent antioxidant activity of polydopamine films: The chemistry-morphology interplay, Colloids Surf. A Physicochem Eng. Asp. 614 (2021) 126134, https://doi.org/10.1016/j.colsurfa.2021.126134.
[46] M. Salomäki, L. Marttila, H. Kivelä, T. Ouvinen, J. Lukkari, Effects of pH and oxidants on the first steps of polydopamine formation: a thermodynamic approach, J. Phys. Chem. B 122 (2018) 6314–6327, https://doi.org/10.1021/acs.jpcb.8b02304.
[47] F. Ponzio, J. Barthès, J. Bour, M. Michel, P. Bertani, J. Hemmerlé, M. D'Ischia, V. Ball, Oxidant control of polydopamine surface chemistry in acids: a mechanism-based entry to superhydrophilic-superoleophobic coatings, Chem. Mater. 28 (2016) 4697–4705, https://doi.org/10.1021/acs.chemmater.6b01587.
[48] J.F. Perez-Benito, Reaction pathways in the decomposition of hydrogen peroxide catalyzed by copper(II), J. Inorg. Biochem 98 (2004) 430–438, https://doi.org/10.1016/j.jinorgbio.2003.10.025.
[49] S. Wang, M. Wahiduzzaman, C. Martineau-Corcos, G. Maurin, C. Serre, A microporous zirconium metal-organic framework based on trans-aconitic acid for selective carbon dioxide adsorption, Eur. J. Inorg. Chem. 2019 (2019) 2674–2679, https://doi.org/10.1002/ejic.201801284.
[50] S. Wang, N. Xhaferaj, M. Wahiduzzaman, K. Oyekan, X. Li, K. Wei, B. Zheng, A. Tissot, J. Marrot, W. Shepard, C. Martineau-Corcos, Y. Filinchuk, K. Tan, G. Maurin, C. Serre, Engineering structural dynamics of zirconium metal–organic frameworks based on natural C4 linkers, J. Am. Chem. Soc. 141 (2019) 17207–17216, https://doi.org/10.1021/jacs.9b07816.
[51] L. Celaya-Azcoaga, A. Crespi, W. Shepard, R. Quezada, M. Luz, P. Ramos, M. Cavallo, I. Irastorza Epelde, H. Garcia Garcia, B. Bazán, F. Bonino, A. García, G.J. Copello, O. Castillo, U. Silván, R. Fernández de Luis, Metal-Organic Chelator

Frameworks for Arsenic-Based Cancer Treatment, n.d. https://ssrn.com/abstract=5007708.
[52] M.J. Cliffe, E. Castillo-Martínez, Y. Wu, J. Lee, A.C. Forse, F.C.N. Firth, P. Z. Moghadam, D. Fairen-Jimenez, M.W. Gaultois, J.A. Hill, O.V. Magdysyuk, B. Slater, A.L. Goodwin, C.P. Grey, Metal–organic nanosheets formed via defect-mediated transformation of a hafnium metal–organic framework, J. Am. Chem. Soc. 139 (2017) 5397–5404, https://doi.org/10.1021/jacs.7b00106.
[53] M. Ermer, J. Mehler, B. Rosenberger, M. Fischer, P.S. Schulz, M. Hartmann, UiO-66 and hcp UiO-66 Catalysts Synthesized from Ionic Liquids as Linker Precursors, ChemistryOpen 10 (2021) 233–242, https://doi.org/10.1002/open.202000291.
[54] A. Valverde, D. Payno, L. Lezama, J.M. Laza, S. Wuttke, R. Fernández de Luis, Multivariate Functionalization of UiO-66 for Photocatalytic Water Remediation, Adv. Sustain Syst. 6 (2022) 2200024, https://doi.org/10.1002/ADSU.202200024.
[55] H. Salazar, M. Rosales, I. Zarandona, J. Serra, B.F. Gonçalves, A. Valverde, L. P. Cavalcanti, S. Lanceros-Mendez, A. García, K. de la Caba, P. Guerrero, P. M. Martins, R. Fernández de Luis, Metal-organic framework functionalized chitosan/pectin membranes for solar-driven photo-oxidation and adsorption of arsenic, Chem. Eng. J. 497 (2024) 154417, https://doi.org/10.1016/j.cej.2024.154417.
[56] K.P. Shearer, G.C. Chavan, S. Bordiga, S. Svelle, S. Olsbye, U. Lillerud, Defect engineering: tuning the porosity and composition of the metal−organic framework UiO-66 via modulated synthesis, Chem. Mater. 28 (2016) 3749–3761, https://doi.org/10.1021/acs.chemmater.6b00602.
[57] K.P. Øien, S. Wragg, D. Reinsch, H. Svelle, S. Bordiga, S. Lamberti, C. Lillerud, Detailed structure analysis of atomic positions and defects in Zirconium Metal − Organic Frameworks, Cryst. Growth Des. 14 (2014) 5370–5372.
[58] A. Valverde, G.I. Tovar, N.A. Rio-López, D. Torres, M. Rosales, S. Wuttke, A. Fidalgo-Marijuan, J.M. Porro, M. Jiménez-Ruiz, V. García Sakai, A. García, J. M. Laza, J.L. Vilas-Vilela, L. Lezama, M.I. Arriortua, G.J. Copello, R. Fernández de Luis, Designing metal-chelator-like traps by encoding amino acids in zirconium-based metal–organic frameworks, Chem. Mater. 34 (2022) 9666–9684, https://doi.org/10.1021/acs.chemmater.2c02431.
[59] M.M. Rodríguez-Delgado, G.S. Alemán-Nava, J.M. Rodríguez-Delgado, G. Dieck-Assad, S.O. Martínez-Chapa, D. Barceló, R. Parra, Laccase-based biosensors for detection of phenolic compounds, TrAC Trends Anal. Chem. 74 (2015) 21–45, https://doi.org/10.1016/J.TRAC.2015.05.008.
[60] H. Liang, F. Lin, Z. Zhang, B. Liu, S. Jiang, Q. Yuan, J. Liu, Multicopper laccase mimicking nanozymes with nucleotides as ligands, ACS Appl. Mater. Interfaces 9 (2017) 1352–1360, https://doi.org/10.1021/ACSAMI.6B15124/ASSET/IMAGES/LARGE/AM-2016-151242_0007.JPEG.
[61] Copper–Oxygen Complexes Revisited: Structures, Spectroscopy, and Reactivity | Chemical Reviews, (n.d.). https://pubs.acs.org/doi/10.1021/acs.chemrev.6b00636 (accessed October 31, 2022)..
[62] P.K. Olshin, O.S. Myasnikova, M.V. Kashina, A.O. Gorbunov, N.A. Bogachev, V. O. Kompanets, S.V. Chekalin, S.A. Pulkin, V.A. Kochemirovsky, M.Yu. Skripkin, A. S. Mereshchenko, The electronic spectra and the structures of the individual copper (II) chloride and bromide complexes in acetonitrile according to steady-state absorption spectroscopy and DFT/TD-DFT calculations, Chem. Phys. 503 (2018) 14–19, https://doi.org/10.1016/j.chemphys.2018.01.020.
[63] R. Vafazadeh, M. Alinaghi, A. Benvidi, A.C. WillisArticle in Acta Chimica Slovenica · March, 2014. https://www.researchgate.net/publication/261069088..
[64] T.F. Pascher, M. Ončák, C. van der Linde, M.K. Beyer, Spectroscopy and photochemistry of copper nitrate clusters, Phys. Chem. Chem. Phys. 23 (2021) 9911–9920, https://doi.org/10.1039/D1CP00629K.
[65] P.K. Bharadwaj, E. John, J.A. Potenza, H.J. Schugar, C.L. Xie, D. Zhang, D. N. Hendrickson, Crystal structure and magnetic properties of the cluster complex Cui2Cuii3[(SCH2CH(C02CH3)NHCH2-)2]3.2C104-H20, a mixed-valence copper-mercaptide species, Inorg. Chem. 25 (1986) 4541–4546, https://doi.org/10.1021/IC00245A018/SUPPL_FILE/IC00245A018_SI_001.PDF.
[66] N. Yoshinari, K. Tatsumi, A. Igashira-Kamiyama, T. Konno, Redox-mediated self-organization of metallosupramolecular architectures composed of D-Penicillaminato CuI8CuII6 clusters: drastic structural change by subtle pH changes, Chem. A Eur. J. 16 (2010) 14252–14255, https://doi.org/10.1002/CHEM.201002780.
[67] B. Bennett, J.M. Kowalski, Chapter Thirteen - EPR Methods for Biological Cu(II): L-Band CW and NARS, in: P.Z. Qin, K.B.T.-M. in E. Warncke (Eds.), Electron Paramagnetic Resonance Investigations of Biological Systems by Using Spin Labels, Spin Probes, and Intrinsic Metal Ions, Part A, Academic Press, 2015, pp. 341–361, https://doi.org/10.1016/bs.mie.2015.06.030.
[68] S.K. Hoffmann, J. Goslar, S. Lijewski, A. Zalewska, EPR and ESE of CuS4 complex in Cu(dmit)2: g-Factor and hyperfine splitting correlation in tetrahedral Cu–sulfur complexes, J. Magn. Reson. 236 (2013) 7–14, https://doi.org/10.1016/j.jmr.2013.08.009.
[69] C. Schöneich, Thiyl radicals: formation, properties, and detection. Redox Chemistry and Biology of Thiols, Elsevier, 2022, pp. 115–132, 10.1016/B978-0-323-90219-9.00001-7.
[70] F. Dénès, M. Pichowicz, G. Povie, P. Renaud, Thiyl radicals in organic synthesis, Chem. Rev. 114 (2014) 2587–2693, https://doi.org/10.1021/cr400441m.
[71] D.A. Stoyanovsky, A. Maeda, J.L. Atkins, V.E. Kagan, Assessments of thiyl radicals in biosystems: difficulties and new applications, Anal. Chem. 83 (2011) 6432–6438, https://doi.org/10.1021/ac200418s.
[72] M.D. Sevilla, D. Becker, M. YanThe formation and structure of the sulfoxyl radicals RSO •, RSOO •, RSO2 •, and RSO200 • from the reaction of cysteine, glutathione and penicillamine thiyl radicals with molecular oxygen1990.
[73] G. Lassmann, M. Kolberg, G. Bleifuss, A. Gräslund, B.M. Sjöberg, W. Lubitz, Protein thiyl radicals in disordered systems: a comparative epr study at low temperature, Phys. Chem. Chem. Phys. 5 (2003) 2442–2453, https://doi.org/10.1039/b302601a.
[74] M. Geoffroy, E.A.C. Lucken, Electron spin resonance spectra of RSO2 radicals formed by the x radiolysis of sulfones, J. Chem. Phys. 55 (1971) 2719–2723, https://doi.org/10.1063/1.1676486.
[75] M.D. Sevilla, D. Becker, S. Swarts, J. HerringtonSULFINYL RADICAL FORMATION FROM THE REACTION OF CYSTEINE AND GLUTATHIONE THIYL RADICALS WITH MOLECULAR OXYGEN1987.
[76] K.A. Lomachenko, A. Martini, D.K. Pappas, C. Negri, M. Dyballa, G. Berlier, S. Bordiga, C. Lamberti, U. Olsbye, S. Svelle, P. Beato, E. Borfecchia, The impact of reaction conditions and material composition on the stepwise methane to methanol conversion over Cu-MOR: an operando XAS study, Catal. Today 336 (2019) 99–108, https://doi.org/10.1016/j.cattod.2019.01.040.
[77] A. Kładna, P. Berczyński, I. Kruk, T. Michalska, H.Y. Aboul-Enein, Scavenging of hydroxyl radical by catecholamines, Luminescence 27 (2012) 473–477, https://doi.org/10.1002/bio.1377.
[78] T. Shimizu, Y. Nakanishi, M. Nakahara, N. Wada, Y. Moro-oka, T. Hirano, T. Konishi, S. Matsugo, Structure effect on antioxidant activity of catecholamines toward singlet oxygen and other reactive oxygen species in vitro, J. Clin. Biochem Nutr. 47 (2010) 181–190, https://doi.org/10.3164/jcbn.09-112.
[79] A. Squarcina, A. Santoro, N. Hickey, R. De Zorzi, M. Carraro, S. Geremia, M. Bortolus, M. Di Valentin, M. Bonchio, Neutralization of reactive oxygen species at dinuclear Cu(II)-cores: tuning the antioxidant manifold in water by ligand design, ACS Catal. 10 (2020) 7295–7306, https://doi.org/10.1021/acscatal.0c01955.
[80] D.B. Rorabacher, Electron transfer by copper centers, Chem. Rev. 104 (2004) 651–698, https://doi.org/10.1021/cr020630e.
[81] D.L. Ross, A.J. Jasniewski, J.W. Ziller, E.L. Bominaar, M.P. Hendrich, A.S. Borovik, Modulation of the bonding between copper and a redox-active ligand by hydrogen bonds and its effect on electronic coupling and spin states, J. Am. Chem. Soc. 146 (2024) 500–513, https://doi.org/10.1021/jacs.3c09983.